Stress-Encoded Mitochondrial Plasticity: ATF4 Control of Mega-Mitochondria and Nanotunnel Communication

Amber Crabtree[1,2,3*], Suraj Thapliyal[4*], Mohd Mabood Khan[5*], Edgar Garza Lopez[6,7], Andrea Marshall[1,7], Calixto Pablo Hernandez Perez[1], Oleg Kovtun[8], Jenny C. Schafer[9], Dea Pulatani[1], Yuho kim[10], Sepiso K Masenga[1,5,11], Annet Kirabo[5], Jeremiah Afolabi[5], Melanie McReynolds[12,13], Renata O. Pereira[14,15,] Prasanna Venkhatesh[4,] Prasanna Katti[4], Brian Glancy[16,17]#, Antentor Hinton, Jr.[1,7]#

1. Department of Molecular Physiology and Biophysics, Vanderbilt University, Nashville, Tennessee, USA.
2. The Frist Center for Autism and Innovation, Vanderbilt University, Nashville, Tennessee, USA.
3. Department of Physics and Astronomy, Vanderbilt University, Nashville, Tennessee, USA.
4. Department of Biology, Indian Institute of Science Education and Research (IISER) Tirupati, AP, 517619, India.
5. Department of Medicine, Division of Genetic Medicine & Clinical Pharmacology, Vanderbilt University Medical Center, Nashville, TN 37232, USA
6. Department of Internal Medicine, Section of Cardiovascular Medicine, Wake Forest University School of Medicine, Winston-Salem, NC 27157 USA
7. Department of Biomedical Sciences, School of Graduate Studies, Meharry Medical College, Nashville, TN 37208-3501, USA
8. Department of Chemistry, Vanderbilt University, Nashville, TN, 37232, USA
9. Department of Cell and Developmental Biology, Vanderbilt University, Nashville, TN, 37232, USA
10. Department of Physical Therapy and Kinesiology, University of Massachusetts Lowell, Lowell, MA, USA.
11. Department of Physiological Sciences, Pathology and Microbiology, HAND, research group, Mulungushi University School of Medicine and Health Sciences, Livingstone, Zambia.
12. The Huck Institutes of the Life Sciences, Pennsylvania State University, University Park, PA, USA
13. Department of Biochemistry and Molecular Biology, Pennsylvania State University, University Park, PA, USA
14. Department of Internal Medicine, University of Iowa Carver College of Medicine, Iowa City, IA, 52242, USA.
15. Fraternal Order of Eagles Diabetes Research Center, Iowa City, IA, 52242, USA.
16. National Heart, Lung, and Blood Institute, National Institutes of Health, Bethesda, MD,
17. National Institute of Arthritis and Musculoskeletal and Skin Diseases, NIH, Bethesda, MD

*These authors share co-first authorship.
#These authors share co-senior authorship.
Corresponding author.

Antentor Hinton, Jr.

Address: 2222 Pierce Avenue, Robinson Research Building 750,
Nashville, TN, 37212, USA; Tel.: 319-383-3095 (A.H Hinton).
E-mail address: antentor.o.hinton.jr@Vanderbilt.Edu

Abstract

Mitochondrial structural plasticity is a critical adaptive response to cellular stress, yet the transcriptional networks governing the formation of specialized mitochondrial architectures remain poorly defined. Here, we identified and demonstrated that activating transcription factor 4 (ATF4), the master regulator of the integrated stress response, directly regulates mitochondrial morphological remodeling through a novel ATF4-NRF1/Nrf2-MFN2 signaling axis. Using serial block-face scanning electron microscopy and three-dimensional reconstruction in *Drosophila* flight muscle, primary myotubes, and human skeletal muscle, we show that overexpression of ATF4 promotes significant mitochondrial elongation, increased cristae concentration, enhanced mitochondrial-endoplasmic reticulum contact site (MERC) formation, and the initiation of Mitochondrial Nanotunnels. In contrast, loss of ATF4 results in mitochondrial fragmentation and impaired aerobic capacity. Chromatin immunoprecipitation sequencing reveals direct ATF4 binding at the promoters of the genes encoding NRF1 and Nrf2, which in turn regulate *MFN2* expression. Small-molecule inhibition studies further establish that activation of this hierarchical pathway is both necessary and sufficient for stress-induced mitochondrial structural adaptation. Together, these findings position ATF4 as a master regulator of mitochondrial architectural plasticity, providing a direct mechanistic link between cellular stress signaling and organelle remodeling.

Keywords: Stress; 3D Structure; Mitochondria; Metabolism; ATF4;

Introduction

Mitochondria are essential organelles that produce cellular energy. However, recent advances in three-dimensional electron microscopy have revealed that these organelles possess substantially greater structural diversity and dynamic nature than the traditional “kidney bean” model. Mitochondrial structure plays an imperative role in determining function, and mitochondrial remodeling is evident in descriptions of distinct morphological phenotypes, which include donuts, Megamitochondria, nanotunnels, and highly branched networks (Vincent, Turnbull et al. 2017, Jenkins, Neikirk et al. 2024). These structural modifications are more than just physical oddities; they are becoming understood to have functional significance, allowing mitochondria to adapt to the cell's changing metabolic, energy, and signaling needs.

Mitochondrial structure and function are highly connected. In addition to producing ATP, mitochondria regulate apoptosis, calcium homeostasis, redox signaling, and metabolic intermolecular coupling (Bratic and Larsson 2013, Del Campo, Contreras-Hernández et al. 2018). Mitochondria possess dynamic properties that include cycles of division mediated by proteins such as dynamin-related protein 1 (DRP1), as well as cycles of fusion mediated by proteins like optic atrophy protein 1 (OPA1) and mitofusin 1/2 (MFN1/2), which help accommodate the cell microenvironment (Chan 2012, Dong and Yao 2022). Any malfunction in these processes can lead to altered mitochondrial morphology and function, contributing to mitochondrial dysfunction in diverse pathological contexts (Bartsakoulia, Pyle et al. 2018)In addition to basal mitochondrial dynamics, mitochondria undergo substantial three-dimensional alterations in response to stress, adopting shapes that illustrate adaptive responses to proteostatic, metabolic, or oxidative stressors. (Glancy 2020).

There is mounting evidence that stress-induced mitochondrial morphologies are functionally specific. For example, although adaptive donut-shaped mitochondria may have a higher surface area to volume ratio, they may be less efficient at producing ATP and more suited for signaling and organelle interactions (Hara, Yuk et al. 2014, Cogliati, Enriquez et al. 2016). Expanded mitochondria-endoplasmic reticulum contact sites (MERCS) promote lipid metabolism, calcium exchange, and stress signaling (Bustos, Cruz et al. 2017). The formation of Megamitochondria is a stress-associated process shared by all organisms and tissues. On the other hand, Mitochondrial

Nanotunnels enable long-range communication between mitochondria (Vincent, Turnbull et al. 2017, Hinton, Claypool et al. 2024, Jenkins, Neikirk et al. 2024). We still don't know the regulatory logic governing the formation of these structures, conserved.

The integrated stress response (ISR) is a conserved signaling pathway that enables cells to adapt to diverse stressors, including endoplasmic reticulum stress, amino acid deprivation, hypoxia, and oxidative stress. The ISR activation leads to the phosphorylation of eIF2α through PERK, GCN2, PKR, or HRI, to trigger global depletion of protein synthesis and selective upregulation of ATF4 expression levels (Pakos-Zebrucka, Koryga et al. 2016). ATF4 is a multifunctional basic leucine zipper master transcriptional regulator, imparting a vital function in integrating the expression of genes involved in amino acid metabolism, antioxidant mechanisms, and autophagy in determining cell fate in a stress state context (Adams, Ebert et al. 2017, Rasmussen and Adams 2020). When activated, ATF4 heterodimerizes with diverse bZIP partners, allowing for combinatorial control.

Recent evidence suggests a possible association between the ISR and mitochondrial structural alterations. ER stress changes the architecture and function of mitochondria by affecting their lipid composition, metabolism, and MERCS (Hinton, Katti et al. 2024). PERK-stimulation of ATF4 has been shown to influence mitochondrial structural remodeling, indicating that ATF4 might function upstream of organelle structural adaptation (Jenkins, Neikirk et al. 2024). Given its critical role in coordinating metabolic and organelle stress responses, ATF4 has the potential to regulate long-term, transcriptionally encoded remodeling of mitochondrial structure. Here, we identify ATF4 as a master transcriptional regulator of mitochondrial architecture. Using three-dimensional electron microscopy, transcriptomics, and functional analyses across *Drosophila* and mammalian systems, we demonstrate that ATF4 orchestrates mitochondrial elongation, cristae densification, MERC expansion, and nanotunnel formation through a conserved NRF1/Nrf2–MFN2 axis (Vincent, Turnbull et al. 2017). We establish that ATF4 directly regulates the expression of nuclear respiratory factor 1 (NRF1), nuclear factor erythroid 2-related factor 2 (NRF2), and MFN, coordinating the formation of specialized mitochondrial structures during cellular stress. This study elucidates a mechanistic framework for understanding how cells employ specialized mitochondrial architectures to sustain cellular homeostasis under environmental stress, demonstrating the evolutionary conservation of this pathway from *Drosophila* to mammals.

Materials and Methods

Fly Model & Genetic Strains

The flies were maintained in vials or bottles on a standard yeast-cornmeal agar medium at 25 °C under a 12-hour light/dark cycle. The W1118 strain was used as the genetic background control for all the fly lines. The Mef2-Gal4 driver was used to achieve muscle-specific gene expression. The muscle-specific knockdown (KD) experiment used Mef2-Gal4 (Bloomington Stock #27390) flies crossed with Tub-Gal80ts at 18°C, which was later raised to 29°C after the larval stage was reached. When manipulating ATF4 signaling, RNAi knockdown and overexpression lines targeting ATF4/cryptocephal (crc) were crossed with Mef2-Gal4. Visualization of mitochondria was conducted using UAS-mito-GFP. All Drosophila stocks were procured from the Bloomington Drosophila Stock Center, and chromosomal designations and gene nomenclature followed FlyBase conventions (http://flybase.org).

Mitochondrial Staining and Confocal Imaging

The thoraces of *Drosophila*, aged between 2-3 days were dissected in 4% paraformaldehyde (PF; Sigma-Aldrich) and indirect flight muscles were isolated as previously stated (Katti, Rai et al. 2021). The isolated muscles were then fixed 4% PF for 1.5 hours under constant stimulation, followed by three 15-minute washes in PBSTx (PBS containing 0.3% Triton X-100). We also used GFP expressed from UAS-mito-GFP under Mef2-Gal4 control. The experimenter labeled F-actin by incubating muscles with 2.5 µg/mL phalloidin-TRITC (Sigma-Aldrich) in PBS for 40 minutes at room temperature. After staining, we mounted the muscles with Prolong Glass Antifade Mountant, with NucBlue (ThermoFisher). Then, we imaged the muscles on a Zeiss LSM 780 microscope.

For the distribution analysis, inside myotubes, we stained the cells with MitoTracker Orange to visualize mitochondrial morphology and subcellular localization. We also used methyl ester (TMRM) to measure the membrane potential to assess mitochondrial function. Spinning-disk super-resolution by Optical Pixel Reassignment (SoRa) microscopy was used to obtain super-resolution images. The intensity of radial fluorescence profiles was quantified across five concentric subcellular zones: nuclear, perinuclear, central, radial, and distal.

To obtain high-resolution z-stacks of live cells stained with MitoTracker Orange or MitoTracker Green/TMRM, confocal images were acquired using a 100× Plan Apo NA 1.45 objective on a spinning disk confocal system based on a Nikon Ti2-E inverted fluorescence microscope equipped with a Yokogawa CSU-W1, Hamamatsu Fusion BT camera, SoRa super-resolution module, environmental chamber, piezo stage controller, and solid-state laser diodes (405, 488, 561, and 640 nm), all controlled using NIS-Elements software (version 5.42; Nikon, Melville, NY). Emission filters were 605/52 nm for the 561 nm channel and 525/36 nm for the 488 nm channel. Serial optical sections were acquired in W1 confocal mode with a 300 nm z-step size.

Drosophila Sample Transmission Electron Microscopy

The dissected samples comprised 2–3-day-old flies fixed with a common fixative solution of 2.5% glutaraldehyde, 1% paraformaldehyde, and 0.12 M sodium cacodylate buffer. Each flight muscle was then isolated and transferred to fresh fixative before processing. Mitochondrial and cristae morphology were manually traced and analyzed using the freehand tool NIH ImageJ software (Schneider, Rasband et al. 2012). Multi-Measure ROI tool in ImageJ was used to make measurements of mitochondrial area, circularity, length, and number (Lam, Katti et al. 2021, Neikirk, Lopez et al. 2023). At identical magnification three specific regions were examined to determine cristae area, circularity index, number, and cristae score. Estimation of cristae volume was conducted by dividing the total cristae area by the total mitochondrial area (Patra, Kwon et al. 2016). Mitochondria-endoplasmic reticulum contact sites (MERCS) were quantified by measuring MERC distance, MERC length, and percentage.

Scanning Transmission Electron Microscope

Sections of epoxy-embedded tissues, measuring 60-80 nm in thickness, were excised using a diamond knife attached to an ultramicrotome (Leica UC7) and then placed on copper grids covered with formvar. To with lead citrate. A scanning transmission electron microscope (STEM) running at 200 kV was used for the imaging. Mitochondrial ultrastructure was visualized using both bright-field (BF) and high-angle annular dark-field (HAADF) detectors. Z-contrast, provided by HAADF imaging, further enhanced visibility. Images were captured at magnifications ranging from

206 20,000× to 150,000×, with pixel sizes of 0.5-2 nm and dwell times per pixel of 1-5 μs to reduce
207 beam-induced damage.
208
209 Mitochondrial morphological metrics, such as length, MERC, were measured using ImageJ for
210 quantitative analysis. The organization of the mitochondrial network was evaluated by measuring
211 its length and branching, and the membrane proximity (<30 nm) was used to identify the
212 mitochondria-ER contact points. With a minimum of three independent samples per condition and
213 ten to twenty mitochondria evaluated per cell, all studies were conducted in a blinded fashion
214 across three or more biological replicates.
215
216 **Animal Models**
217
218 We used male C57BL/6J mice (n = 5-7) as animal models in each age group. We produced $Atf4^{fl/fl}$
219 mice using the procedures that were previously described (Ebert, Dyle et al. 2012). Dr. Pierre
220 Chambon of the University of Strasbourg generously donated the tamoxifen-inducible HSA-
221 CreERT2 mice. The $Atf4^{fl/fl}$ mice were generated by crossing Atf4 with HSA-CreERT2 mice. The
222 mice were given free access to food and water and kept in a typical environment with a 12-hour
223 light-dark cycle. The mice were euthanized using cervical dislocation followed by CO_2 anesthesia.
224 All serum samples were collected between 8:00 am and 12:00 pm. Total body weight was
225 measured at the time of tissue collection. All animal-related procedures were conducted in
226 compliance with the standards set forth by the institutional animal care and use committee.
227
228 **Primary Cell Culture**
229
230 Satellite cells were isolated following previously verified methods (Pereira, Tadinada et al. 2017).
231 Culture dishes coated with BD Matrigel were used to plate primary satellite cells that were
232 extracted from $Atf4^{fl/fl}$ mice (n = 8 for eachisolated from Atf4fl/fl mice (n = 8 per experimental
233 condition). Isolated cells were then plated on BD Matrigel-coated dishes and cultured in
234 DMEM/F-12 medium (Gibco, Waltham, MA). The plates were subsequently supplemented with
235 20% fetal bovine serum (FBS; Gibco), 40 ng/mL basic fibroblast growth factor, 1× non-essential
236 amino acids, 0.14 mM β-mercaptoethanol, 1% penicillin/streptomycin, and 300 μL/100 mL
237 Fungizone. After plating was complete, the growth factor concentration for basic fibroblast growth

238 factor was reduced to 10 ng/mL to maintain it. When 90% confluency was reached, differentiation
239 was activated by switching DMEM/F-12 containing 2% FBS and 1× insulin-transferrin-selenium.
240
241 Three days after differentiation, myotubes were infected with an adenovirus expressing GFP-Cre
242 to generate ATF4 knockout (ATF4 KO) myotubes. An ATF4-expressing adenovirus (Ad5CMV-
243 ATF4/RSVeGFP) was used to infect differentiated myotubes to produce ATF4 overexpression
244 (ATF4 OE) for gain-of-function studies. Measurements for all experiments were performed at 3
245 and 7 days post-viral infection. The culture medium was replaced on alternating days by washing
246 with phosphate-buffered saline (PBS) to remove residual media. Maintenance of C2C12 myoblasts
247 was carried out at 37°C in a humid atmosphere containing 5% CO2. The growth medium consisted
248 of DMEM containing 4.5 g/L glucose supplemented with 10% fetal bovine serum. The medium
249 was replaced with DMEM containing 2% horse serum after the cells reached confluency to induce
250 differentiation into myotubes. After five days of differentiation initiation, the myotubes were
251 treated with either ethanol, 0.1 μM oligomycin, or 1 μg/mL tunicamycin ± 500 μM 4-phenylbutyric
252 acid (PBA) for 8 hours.
253
254 **Murine and Human Sample Transmission Electron Microscopy**
255 Cells were fixed in 2.5% glutaraldehyde in sodium cacodylate buffer for a period of 1 hour at 37°C
256 as per the previous protocols (Hinton, Katti et al. 2023). Fixed samples were further embedded in
257 2% agarose, post-fixed in 1% osmium tetroxide in buffer, and stained with 2% uranyl acetate.
258 using a graded series of ethanol. Resin embedding was done using EMbed 812. Sections of 80 nm
259 thickness were prepared by an ultramicrotome and stained with 2% uranyl acetate and lead citrate.
260 Microscopy was carried out on a JEOL JEM-1230 transmission electron microscope at an
261 acceleration voltage of 120 kV.
262
263 **Serial Block Face-Scanning Electron Microscopy**
264 We have prepared the samples according to previously published protocol (Garza-Lopez, Vue et
265 al. 2021, Vue, Neikirk et al. 2023). The tissue samples were fixed in a 2% glutaraldehyde solution
266 dissolved in 0.1 M cacodylate buffer before heavy metal staining, as previously published
267 (Mustafi, Kikano et al. 2014). The samples underwent a sequential process that started with a 3%
268 potassium ferrocyanide solution containing 2% osmium tetroxide at 4°C for 1 hour. The samples

were filtered after the thiocarbohydrazide solution at 0.1% concentration was applied for 20 minutes. The samples were treated for 30 minutes with a 2% osmium tetroxide solution, then placed in 1% uranyl acetate solution for overnight storage at 4°C. The process required deionized water washes to be performed between each step. The following day, samples were treated with 0.6% lead aspartate solution (30 minutes at 60°C) and dehydrated through graded acetone dilutions. Tissues were infiltrated with TAAB 812 hard epoxy resin (Aldermaston, Berks, UK), embedded in fresh resin, and polymerized at 60°C for 36-48 hours. Following polymerization, blocks were sectioned for transmission electron microscopy to identify regions of interest, then trimmed to 0.5 mm × 0.5 mm and mounted on aluminum pins. Pins were placed in a scanning electron microscope for serial block-face imaging. Images were collected from 300-400 thin (0.09 µm) serial sections for three-dimensional reconstruction.

3D Reconstruction and Segmentation

Three-dimensional reconstruction of serial block-face scanning electron microscopy data was performed according to conventional protocols (Crabtree et al., 2023; Garza-Lopez et al., 2022; Hinton et al., 2023; Neikirk et al., 2023; Vue et al., 2023). A volume of data, approximately 300-400 orthoslices thick, comprising 50-100 sections was assembled for reconstruction in Amira software (ThermoFisher Scientific). An investigator blinded to experimental conditions and experienced organelle identification manually segmented structural features by tracing contours through sequential slices of micrograph blocks using contour-tracing tools. The resulting volumetric structures were quantified and assembled into three-dimensional visualizations (Garza-Lopez, Vue et al. 2021). For *Drosophila* samples, Imaris image analysis software was additionally employed for 3D reconstruction and volumetric quantification of mitochondrial networks.

Western Blotting

Protein extracts isolated from differentiated myotubes as well as C2C12 cells, were obtained following approved protocols (Hinton, Katti et al. 2024). Cold PBS was used to wash cells, which were subsequently lysed in a cold lysis solution containing 25 mM Tris-HCl pH 7.9, 5 mM MgCl2, 10% glycerol, 100 mM KCl, 1% NP-40, 0.3 mM dithiothreitol, 5 mM sodium pyrophosphate, 1 mM sodium orthovanadate, 50 mM sodium fluoride, and a protease inhibitor cocktail. After lysis, cells were scraped from culture dishes, homogenized with a 25-gauge needle, and centrifuged at

300 14,000 rpm (5,268 × g) for 10 minutes at 4°C. Supernatants, were then diluted with Laemmli
301 sample buffer to 1× concentration.
302
303 Protein was isolated by sodium dodecyl sulfate-polyacrylamide gel electrophoresis and transferred
304 to nitrocellulose membranes (Bio-Rad, Berkeley, CA). Membranes were blocked using a solution
305 of 5% bovine serum albumin in Tris-buffered saline containing 0.05% Tween-20. The primary
306 antibodies that were used were BIP (BD Biosciences, #610978, 1:5,000), GRP75 (Cell Signaling
307 Technology, #D13H4, 1:1,000), VDAC (Cell Signaling Technology, #4866, 1:1,000), ATF4
308 (Proteintech, Rosemont, IL, 10835-1-AP, 1:1,000), IP3R3 (BD Biosciences, #610312, 1:1,000),
309 FGF21, OPA1 (BD Biosciences, San Jose, CA, #612606, 1:1,000), DRP1, MFN-1 (Abcam,
310 Cambridge, UK, ab57602, 1:1,000), and MFN-2 (Abcam, ab101055, 1:1,000). GAPDH (Cell
311 Signaling Technology, Danvers, MA, #2118, 1:5,000) and actin served as loading controls. For the
312 secondary antibodies Alexa Fluor anti-rabbit 680 (Invitrogen, #A27042, 1:10,000) was included.
313 The respective protein bands observed were quantified using Image Studio Lite Ver 5.2 software.
314
315 **RNA Extraction and Quantitative Real-Time PCR**
316
317 RNA was extracted from the cells by employing the RNeasy Kit, as recommended by the supplier
318 (Qiagen Inc.). Concentration and purity of RNA were determined by analyzing A260/A280 values
319 by employing the NanoDrop 1000 spectrophotometer (NanoDrop Products, Wilmington, DE).
320 Reverse transcriptions of 1 μg isolated RNA were performed by employing the High-Capacity
321 cDNA Reverse Transcription Kit (Applied Biosystems, Carlsbad, CA), as earlier described
322 (Boudina, Sena et al. 2007).
323
324 Real-time q-PCR was conducted employing SYBR Green dye (Life Technologies Inc.; Carlsbad,
325 CA). The samples in each experimental group were run in triplicates with approximately 50 ng of
326 cDNA per reaction, in a 384-well plate format, employing ABI Prism 7900 HT sequencing
327 detection systems (Applied Biosystems). The cycling thermal profiles began with a denaturation
328 step of 10 minutes at 95°C, followed by 40 cycles of amplification, each consisting of 15 seconds
329 at 95°C, 15 seconds at 59°C, and finally an extension of 30 seconds at 72°C. Gene expression was
330 determined by ΔΔCt analysis, normalized to GAPDH expression.
331

332 For *Drosophila* samples, RNA was isolated from the flight muscles of 1-2-day-old flies. We
333 removed the flight muscles from cut thoraces at 4 °C. Placed the flight muscles, in TRIzol reagent
334 (Sigma-Aldrich/Invitrogen). We extracted the RNA with a tissue grinder. Reverse transcription of
335 the RNA was performed using SuperScript III (Invitrogen). For RT-PCR we used 50 ng of cDNA
336 per reaction. For RT-PCR we mixed the cDNA with iTaq Universal SYBR Green (Bio-Rad). Ran
337 the reaction, on a QuantStudio 6 Flex system (Applied Biosystems).
338
339 **RNA Sequencing and Bioinformatic Analysis**
340 Sequencing of RNA was done following previously established protocols (Hall, Medina et al.
341 2017). For *Drosophila* studies, RNA was isolated from five wild-type and five ATF4 knockdown
342 flies. The sequencing reads were uploaded to Kallisto and quantified using Kallisto (v0.46.2) with
343 an index built from BDGP6.28 genome assembly transcript sequences. Differential gene
344 expression analysis was conducted using DESeq2 (v1.30.0). Gene list that exhibited expression
345 levels greater than 5 fragments per kilobase per million reads were compiled and classed in either
346 control or ATF4 knockdown samples.
347
348 For the mammalian cell line analysis, genes with differential expressions were found with the filter
349 criterion of the absolute log2 fold change > 0.66 and an adjusted p-value < 0.05. For enrichment
350 analyses, the tool used was Ingenuity Pathway Analysis (IPA) and WebGestalt for Gene Set
351 Enrichment Analysis (GSEA). For IPA and GSEA, significance was assessed using the following:
352 IPA: an adjusted p value of < 0.05. GSEA: an absolute Z-score of > 2 with an adjusted p value of
353 < 0.05, and an absolute enrichment score of > 2. The PANTHER database (http://pantherdb.org/)
354 was utilized to evaluate Gene Ontology data, whereas WebGestalt (http://www.webgestalt.org/)
355 was used for pathway analysis, looking for KEGG pathways, and searching the gene promoters
356 for binding sites of every transcription factor.
357
358 **Chromatin Immunoprecipitation Sequencing**
359 ChIP-sequencing was performed following a 10-hour treatment with tunicamycin (2 µg/mL) in
360 $Atf4^{+/+}$, $ATF4^{-/-}$, $Chop^{+/+}$, and $Chop^{-/-}$ MEFs, as described in previous literature (Han, Back et al.
361 2013, Tameire, Verginadis et al. 2019, Zou, Ohta et al. 2022). The DNA fragments obtained were
362 processed for sequencing, which was performed according to the protocol. The peaks for ATF4

363 and CHOP binding at gene promoters were identified using standard peak identification
364 algorithms.
365
366 **Mitochondrial Respiratory Function**
367 Cell metabolism measurements were performed by using an XF24 Extracellular Flux Analyzer
368 (Agilent Technologies-Seahorse Bioscience, North Billerica, MA), seeding a final concentration
369 of 20,000 cells/well and differentiation as described above. On day three post-differentiation, cells
370 were infected with adenoviruses expressing ntGFP and/or GFP-Cre at a high MOI calculated to
371 achieve infection efficiencies higher than 95% as determined by fluorescence intensity. On day
372 three post-infection, XF culture medium replaced regular culture medium, and the cells were
373 placed in a non-CO_2 incubator for 60 minutes.
374
375 The rate of basal oxygen consumption rate (OCR) was assessed using XF-DMEM, after which
376 additional assessments of OCR were conducted in response to the following compounds added
377 into the medium: oligomycin (1 μg/mL) to estimate ATP-linked respiration, FCCP (1 μM) to
378 estimate maximum respiratory capacity, and a combination of rotenone (1 μM) and antimycin A
379 (10 μM) to estimate non-mitochondrial respiration (Wende, O'Neill et al. 2015). The spare
380 respiratory capacity was then calculated by subtracting basal OCR from maximum OCR.
381
382 **Measurement of Mitochondria Membrane Potential and Reactive Oxygen Species**
383 The mitochondrial membrane potential was assessed using the fluorescent cationic dye
384 tetramethylrhodamine methyl ester (TMRM). The quantification of TMRM fluorescence intensity
385 loss over time within a given microscopic field was performed. The production of mitochondrial
386 hydrogen peroxide was measured using MitoPeroxy Yellow 1 (MitoPY1). The TMRM
387 fluorescence was quantified using the FIJI/ImageJ (NIH) method. The time-lapse image stacks
388 were initially imported and, if needed, drift was corrected using the StackReg/TurboReg plugin.
389 Regions of interest (ROIs) belonging to particular cells or mitochondrial-rich areas were manually
390 identified and the mean fluorescence intensity for each ROI was calculated at all time points. All
391 data were adjusted for background fluorescence, which was calculated from areas devoid of cells.
392 To get the relative changes in mitochondrial membrane potential over time (F/F_0), the intensity
393 values of the fluorescence were normalized to the original baseline fluorescence (F_0). Data from

394 several ROIs and separate experiments were averaged for population analysis, and the fluorescence
395 decay rate was determined to quantify mitochondrial depolarization kinetics. The data are
396 represented as mean ± standard error of the mean from at least three separate experiments for each
397 experimental group, with four fields per well at various time points.
398
399 **Calcium Imaging**
400 Intracellular calcium dynamics were assessed in primary mouse myotubes using Fura-2 AM, a
401 ratiometric imaging technique that alternates excitation at 340 nm and 380 nm, with emission at
402 510 nm. Calcium transients were induced and recorded over a time period of 300 seconds. Peak
403 amplitude and area under the curve were quantified to assess calcium handling capacity across
404 experimental groups.
405
406 **Statistical Analysis**
407 Results are expressed as mean values ±SE of mean. If two groups were compared, unpaired
408 Student's *t* tests were employed. For more than two groups, one-way or two-way analysis of
409 variance tests were applied, followed by posttests of either Tukey's multiple comparisons or
410 Fisher's protected least significant difference tests. Statistical analyses were performed using from
411 SAS Institute. The level of significance in all analyses was fixed at $p < 0.05$, as marked: *$p < 0.05$,
412 **$p < 0.01$, ***$p < 0.001$, ****$p < 0.0001$
413
414
415 **Results**
416
417 **ATF4 expression alters mitochondrial morphology in *Drosophila* flight muscle**
418 To define mitochondrial organization across spatial scales, we combined Serial Block-Face
419 Scanning Electron Microscopy (SBF-SEM) with confocal fluorescence imaging of intact tissue
420 (Figure 1). High-resolution volumetric information on mitochondrial morphology was provided
421 by SBF-SEM reconstructions (cyan), and assessment of mitochondrial alignment relative to the
422 contractile apparatus was made possible by confocal imaging of mito-GFP (green) and phalloidin-
423 FITC-labeled myofibrils (red). Figure 1A-C shows the results of three-dimensional SBF-SEM
424 reconstructions revealing mitochondrial morphologies. Mitochondria in the control tissue were
425 arranged in parallel sheets, parallel to the contraction axis, forming a dense, continuous network

426 (Figure 1A). Rotated and orthogonal images (Figure 1A′, A″) showed a densely linked
427 mitochondrial reticulum covering numerous sarcomeres, with limited vacant space and
428 considerable mitochondrial connectivity. In contrast, mitochondria in the KD model exhibited
429 pronounced structural disruption. The mitochondrial networks were found to be thin and
430 perforated (Figure 1B), resulting in a porous, lattice-like structure. A loss of planar order and
431 increased fragmentation were seen across the volume in the orthogonal views (Figure 1B′, B″).
432 Figure 1C clearly shows a remodeling phenotype, with mitochondria looking stacked and
433 expanded, creating thickened lamellar structures. In contrast to the controls, the rotated images
434 (Figure 1C′, C″) exhibited reduced network connectivity but retained partial alignment with the
435 contraction axis.
436
437 The SBF-SEM-identified ultrastructural characteristics were confirmed by confocal imaging
438 (Figure 1E-G, Video1-12). To confirm the presence of planar mitochondrial sheets, mito-GFP-
439 labeled mitochondria in control tissue (Figure 1E) organized into long, highly ordered arrays that
440 closely tracked the direction of actin filaments. The mitochondrial architecture observed in the
441 ATF4 KD group was characterized by a fragmented, punctate mito-GFP signal distributed
442 unevenly across myofibrils in the disrupted samples (Figure 1F). Figure 1G shows that samples
443 from the ATF4 OE groups exhibited expanded mitochondrial structures, with a thick, tightly
444 aligned mito-GFP signal aligned with the contractile axis. The quantitative analysis of
445 mitochondrial volume (Figure 1H) and length (Figure 1I) shows that they are increased in ATF4
446 OE and decreased in ATF4 KD, whereas sphericity (Figure 1J) is increased in ATF4 KD and
447 decreased in ATF4 OE.
448 These findings indicate that genetic modulation of ATF4 expression induces distinct remodeling
449 states characterized by fragmentation or hypertrophic stacking, both of which are detectable by
450 confocal imaging but most clearly defined by volumetric electron microscopy. Collectively, these
451 data validate a multiscale imaging approach for linking mitochondrial ultrastructure to mesoscale
452 tissue organization.
453
454 **ATF4 expression alters mitochondria, MERCS, and gene expression in *Drosophila* flight**
455 **muscle**

456 Transmission electron microscopy (TEM), S/TEM, SBF-SEM, and confocal fluorescence imaging
457 were utilized to determine the effects of ATF4 signaling on mitochondrial structure and
458 connectivity in 2-dimensions versus the 3-dimensions examined in Figure 1 (Figure 2). Using this
459 multiscale method, we were able to quantitatively evaluate the morphology of mitochondria, the
460 organization at higher levels, and the connectivity mediated by nanotubes in different events.

461 ***ATF4 loss and overexpression induce distinct mitochondrial ultrastructural phenotypes***

462 When ATF4 levels were altered, conventional TEM imaging showed significant changes in
463 mitochondrial morphology with varying ATF4 expression levels in *Drosophila* indirect flight
464 muscle (Figure 2A-C"). Mitochondria from our control group (Figure 2A-A″) were long and
465 uniform in size, aligned with myofibrils, and displayed an undamaged cristae configuration. As
466 seen in Figure 2B-B″, mitochondria from our ATF4 knockdown (ATF4 KD) group appear smaller
467 and have a significantly higher circularity index (Figure 2 G, H), with increased cristae surface
468 area and a decreased number of cristae, suggesting a possible disturbance in mitochondrial
469 bioenergetics. Remarkably, mitochondria appear significantly larger and more elongated with
470 ATF4 OE (Figure 2C-C″). This mitochondrial enlarged phenotype, or formation of
471 Megeamitochondria, has been linked to increased metabolic function and stress-responsive
472 mitochondrial remodeling; these mitochondria, which crossed numerous sarcomeres, displayed the
473 characteristic enlarged volume and cross-sectional area previously seen by others with the use of
474 chemically induced cellular stress models. The uneven arrangement of cristae inside these larger
475 mitochondria, rather than a consistent enlargement, suggested structural adaptation taking place
476 over time. Quantifications of these structural changes (Figure 2D-I) indicates that the size, shape,
477 and density of the mitochondria evolved significantly in response to overexpression of ATF4. In
478 contrast to ATF4 OE mitochondria, there was an increase in area and a decrease in aspect ratio in
479 ATF4 KD mitochondria, suggesting that ATF4 plays a role in the maintenance of mitochondrial
480 structural integrity, even without the presence of stress.
481

482 ***SBF-SEM reveals altered mitochondria-ER contact sites (MERCS) with modulation of ATF4***
483 ***expression***

484 Next, we sought to determine whether the formation of MERCS was altered by manipulating ATF4
485 expression (Figure 2J-L). We found that although MERC length increases with both ATF4 KD

(Figure 2 K) and OE (Figure 2 L) relative to control (Figure 2 J, M), MERC distance, however, significantly increased with ATF4 KD and significantly decreased with OE (Figure 2 J-L, N). These data indicate that although MERC length increases with loss of ATF4 and ATF4 OE, the distance between juxtaposed organelles increases with KD and decreases with OE, reflecting decreased and increased MERC tethering, respectively (Figure 2 J-O).

Confocal imaging and SBF-SEM reveal an increased prevalence of Mitochondrial Nanotunnels with alterations in ATF4 expression

Throughout our investigation into how the expression and loss of ATF4 alters mitochondrial structure, we observed considerable alterations in the formation of thin, double-membrane bound protrusions that connect the matrix of the involved mitochondrion, called nanotunnels (Figure 2 P-U", Video13-15). Specifically, the loss of ATF4 significantly alters mitochondrial morphology and produces distinct and highly organized, stereotypically textbook-like nanotunnel structures (Figure 2 U-U"). The thin mitochondrial protrusions observed with ATF4 KD resemble those described in metabolically restricted and stressed and may represent an adaptive effort to maintain organelle-organelle communication during impaired proteostasis and aberrant metabolic regulation. In contrast, the overexpression of ATF4 leads to the mitochondrial expansion and the formation of megamitochondria that remain contiguous through distinguishable nanotunnel-like bridges (Figure 2 P-Q'''; a closer look with nanotunnels indicated by arrowheads shown in (R) and SBF-SEM images of nanotunnels shown in (R')).Quantifications of these changes indicate that nanotunneling increases significantly with both ATF4 KD and OE compared with control flight muscle (Figure 2 P-Y). Although both the loss of and the overexpression of ATF4 relative to control lead to an increase in the prevalence of nanotunnels, these structures provide a means for the formation of extended mitochondrial networks through physical, elongated tubular connections joining adjacent mitochondria, suggesting enhanced content exchange and intra-mitochondrial communication.

Importantly, although these two nanotunnel phenotypes appear anatomically distinct, they may share essential functional similarities; both conditions likely reflect altered mitochondrial remodeling and stress states, potentially involving alterations in mitochondrial cristae structure, lipid metabolism, the distribution of mitochondrial DNA and the regulation of intra-organelle contacts. Thus, ATF4 levels may attune mitochondrial network plasticity, shifting between the

517 compensatory formation of nanotunnels with loss-of-function and the hyperconnectivity of
518 megamitochondria observed with gain-of-function.
519
520 **SBF-SEM reveals ATF4-dependent shifts in mitochondrial size and shape distributions**
521 Mitotyping of individual mitochondria from wild-type, ATF4 KD, and ATF4 *Drosophila* OE
522 indirect flight muscle (IFM) showed different physical characteristics dependent on ATF4
523 expression levels (Figure 3A). Highly oxidative flight muscle is characterized by a limited
524 distribution of elongated, evenly sized mitochondria, which was observed in WT IFM
525 mitochondria. On the other hand, mitochondrial morphologies in ATF4 KD IFM shifted toward
526 smaller, rounder shapes (Figure 3A, F), suggesting disturbed mitochondrial homeostasis. Notably,
527 ATF4 OE IFM showed a wide range of mitochondrial morphologies, including mitochondria that
528 were significantly longer and wider and had a higher volume, which is compatible with
529 mitochondrial expansion and the development of structures similar to Megamitochondria (Figure
530 3 A-F). These mitotyping results indicate that ATF4 expression significantly affects mitochondrial
531 size, shape, and variability in *Drosophila* IFM.
532
533 ***ATF4-dependent mitochondrial remodeling is coupled with transcriptional and metabolic***
534 ***reprogramming***
535 After observing consistent mitochondrial morphology changes with manipulation of ATF4
536 expression, we sought to understand better the implications of these changes at both transcriptional
537 (Figure 3 G-J) and metabolic (Figure 3 K) levels. We utilized RNA-sequencing to look at possible
538 changes at the transcriptome level with alterations in ATF4 expression. According to heatmap
539 analysis, genes related to mitochondrial dynamics, oxidative metabolism, stress-responsive
540 signaling, and quality control pathways showed coordinated expression changes in ATF4 OE.
541 Additional evidence from metabolomic profiling showed that ATF4-dependent remodeling of core
542 metabolic pathways also occurred (Figure 3K). There were changes in metabolites linked to
543 glycolysis, the tricarboxylic acid cycle, amino acid metabolism, and redox balance in ATF4 OE
544 samples, which separated them from WT and ATF4 KO samples. These alterations are in line with
545 the hypothesis that ATF4 expression in *Drosophila* IFM leads to increased mitochondrial mass and
546 a response to different energy demands.
547

548 **ATF4 links mitochondrial architecture to calcium homeostasis in myotubes**
549
550 To examine the functional implications of our observed mitochondrial morphology and nanotunnel
551 changes in a mammalian system, we examined primary mouse WT, ATF4 KO, and ATF4 OE
552 myotubes from $ATF4^{fl/fl}$ mice (Figure 4). Using fluorescent (Figure 4 A-C) and TEM (Figure 4 D-
553 G) imaging, we consistently observed successful infection with adenovirus expressing GFP
554 (control; A), cre-recombinase with a GFP reporter (ATF4 KO; B), and ATF4 adenovirus with a
555 GFP reporter (C). Looking at the mitochondrial level via TEM images, we found that a loss of
556 ATF4 resulted in significant decreases in mitochondrial area and cristae score (or the quality of
557 cristae present), with concomitant increases in MERC distance, suggesting a loss or decrease in
558 MERC tethering relative to control (Figure 4D, E, H-J). Alternatively, the overexpression of ATF4
559 resulted in significant increases in mitochondrial area and cristae score relative to control and
560 concomitant decreases in MERC distance, indicating an increase in MERC tethering (Figure 4 F-
561 J). To better understand how these MERC changes might alter calcium homeostasis, we used the
562 radiometric dye, Fura-2 AM, to measure cytosolic calcium dynamics (Figure 4K-M). In all
563 situations, stimulation caused cytosolic calcium levels to spike quickly, but the response's intensity
564 and rate of elevation were heavily dependent on ATF4 (Figure 4K). Peak calcium amplitude
565 quantification showed that ATF4-deficient and ATF4 OE myotubes had significantly lower peak
566 cytosolic calcium levels than the control group (Figure 4K, L). Area under the curve (AUC)
567 analysis showed that cumulative calcium signal was much higher in ATF4 deletion compared to
568 control, but ATF4 overexpression was not significantly different from control (Figure 4M),
569 suggesting that ATF4 absence altered buffering and calcium clearance dynamics. Taken together,
570 these data indicate that ATF4 expression alters mitochondrial size, MERC distance, and cytosolic
571 calcium handling in mouse primary myotubes.
572

573 **SBF-SEM reveals ATF4-dependent remodeling of MERC volume and length in 3D**
574 To determine if the MERC changes we observed in our mammalian system for control, ATF4 KO,
575 and ATF4 OE in 2-dimensions were consistent in 3-dimensions, we utilized SBF-SEM
576 reconstructions (Figure 5A-C'). Similar to our observed results in 2-dimensions, ATF4 KO showed
577 significantly decreased MERC volume and MERC length (Figure 5 B-B', D, E) relative to control
578 (Figure 5 A-A', D, E) In contrast to our ATF4 KO model, but consistent with our 2D findings,

579 ATF4 OE resulted in significantly increased MERC volume and MERC length when compared to
580 control (Figure 5 A-A', C-C', D, E). These findings are consistent with previous reports that MERC
581 tethering is ATF4-dependent in OPA1-deficient myotubes (Hinton, Katti et al. 2024).
582
583 ***ATF4 overexpression increases mitochondrial volume in primary myotubes***
584 To assess if mitochondrial parameters changed in a consistent manner with MERC changes, we
585 utilized SBF-SEM reconstructions for volumetric analysis (Figure 5 F-L) from ATF4$^{fl/fl}$ primary
586 mouse myotubes. Consistent with our previous findings, we found that ATF4 OE myotubes had a
587 significantly larger mitochondrial volume when compared to (Figure 5 F-L). These findings are
588 also consistent with the appearance of larger structures resembling Megamitochondria and indicate
589 that the increase is due to mitochondrial expansion rather than simple redistribution. Taken
590 together, these results show that ATF4 controls the number and architecture of mitochondria and
591 the mitochondria-ER interface in a coordinated manner.
592
593 To look at these mitochondrial changes at a higher resolution we utilized STED super-resolution
594 imaging in C2C12 myotubes (Figure M-N). Quantifications of these findings show that both
595 mitochondrial area and volume significantly increase with ATF4 overexpression (Figure O, R). To
596 look at these changes in a live-cell model, we utilized spinning-disk confocal SORA imaging of
597 primary mouse myoblasts (Figure P-Q"). The mitochondrial networks in ATF4 OE myotubes
598 appear more robust and elongated or hyperfused as indicated by MitoTracker (Figure P', Q').
599 Cumulatively, these data show that ATF4-dependent mitochondrial remodeling is robust in C2C12
600 and primary mouse myoblasts and myotubes and that these findings are readily observable using
601 live-cell imaging.
602
603 **ATF4 expression alters genes associated with mitochondria and MERCS in *Drosophila* flight**
604 **muscle**
605 To define the transcriptional programs downstream of ATF4 that may underlie the structural and
606 functional mitochondrial phenotypes observed in vivo, we performed untargeted RNA sequencing
607 on *Drosophila* muscle under ATF4 loss- and gain-of-function conditions (Figure 6).
608
609 ***ATF4 loss induces widespread transcriptional reprogramming in fly muscle***

610 Figure 6 A-B shows the results of a comparative analysis between ATF4 KD and control muscles,
611 which showed significant differences in transcription. Analysis of scatter plots comparing the
612 ATF4 KO and control groups showed that gene expression shifted widely after ATF4 deletion, with
613 1,715 genes upregulated and 1,316 downregulated (Figure 6A). In a coordinated manner, genes
614 related to mitochondrial structure and organelle communication, such as the MERC protein
615 machinery and MICOS complex components, were downregulated, as determined by differential
616 expression analysis. Volcano plot analysis provided additional evidence that transcripts related to
617 mitochondrial dynamics, calcium handling, and organelle stress responses are significantly
618 reduced in ATF4 KO muscle (Figure 6B). It has been observed that genes related to mitochondrial
619 quality control, MICOS organization, and MERCS were inversely affected, indicating that ATF4
620 is necessary for the maintenance of transcriptional programs that promote mitochondrial
621 architecture and organelle-organelle communication.
622
623 ***ATF4 overexpression activates stress-responsive and organelle remodeling pathways***
624 Alternatively, a different transcriptional signature was observed in fly muscle with ATF4 OE
625 (Figure 6C-D). Transcripts linked to autophagy-related pathways, unfolded protein response
626 (UPR/ER stress), and mitochondria-ER interactions were significantly overrepresented in the
627 upregulated genes identified by scatter plot analysis (Figure 6C). The volcano plots demonstrated
628 strong activation of canonical ATF4 target pathways, which encompass genes involved in ER stress
629 signaling, adaptive metabolic remodeling, and mitochondrial calcium handling (Figure 6D).
630 Crucially, ATF4 OE muscle showed a specific upregulation of many MERC- and MICOS-
631 associated genes, which allowed us to understand the transcriptional basis of the mitochondrial
632 remodeling and increased MERC architecture we observed with SBF-SEM, STED, and confocal
633 imaging.
634
635 ***Aggregated pathway and gene set enrichment analyses identify ATF4 as a central regulator of***
636 ***mitochondrial–ER communication networks***
637
638 Figure 6E-G shows differential analysis reports for the ATF4 KO and ATF4 OE groups. These
639 findings indicate that ATF4 regulates genes associated with mitochondrial structure, organelle-
640 organelle contact formation, stress adaptation, and quality control. ATF4 acts as a transcriptional

641 regulator, that modulates mitochondrial-ER communication, and stress-responsive remodeling is
642 supported by the reciprocal regulation of genes related to MERCS, MICOS organization, calcium
643 transport, and autophagy in response to ATF4 status. In line with the reported phenotypes of altered
644 MERC size, mitochondrial volume expansion, and calcium-handling abnormalities, pathway-level
645 analysis revealed coordinated modulation of the mitochondrial calcium uptake machinery,
646 endoplasmic reticulum stress sensors, and genes associated with autophagy. These RNA-seq
647 results show that ATF4 is a master transcriptional regulator in fly muscle, linking the biology of
648 organelle contact sites, mitochondrial architecture, and cellular stress adaptation.
649

650 **ATF4 expression reciprocally alters mitochondrial bioenergetics and gene expression levels**
651 **in primary mouse myotubes**

652 To better understand the energetic functional implications at the mitochondrial level of ATF4
653 expression modulation, we utilized untargeted metabolomics and Seahorse extracellular flux
654 analysis to measure oxygen consumption rates (OCR) in primary mouse myotubes. We found that
655 the control, ATF4 KO, and ATF4 OE groups exhibit different metabolic states dependent on the
656 expression of ATF4 (Figure 7A). The metabolic pathways related to amino acids, carbohydrates,
657 and mitochondria were shown to undergo extensive alterations, as shown by differential metabolite
658 analysis (Figure 7B).
659

660 Metabolites associated with redox, glycolytic intermediates, and the tricarboxylic acid (TCA)
661 cycle were among those that underwent alterations, as shown by heatmap visualization of
662 significantly changed metabolites (Figure 7C). Additionally, metabolic pathways linked to amino
663 acid biosynthesis, stress-responsive metabolic adaptability, and mitochondrial energy metabolism
664 were shown to be significantly overrepresented in the pathway enrichment analysis (Figure 7D).
665 Using a Seahorse extracellular flow analysis to assess if metabolic reprogramming resulted in
666 functional mitochondrial alterations. In control myotubes, ATF4 overexpression greatly enhanced
667 baseline and maximal oxygen consumption rates, whereas ATF4 deletion diminished respiratory
668 capacity (Figure 7E-G). The results show that ATF4 increases mitochondrial oxidative capacity,
669 which is consistent with the expanded organelle networks and larger mitochondrial volume
670 observed in EM and super-resolution imaging. Further investigation into spare respiratory capacity
671 revealed that ATF4 OE myotubes maintain greater bioenergetic flexibility than ATF4-deficient

672 cells, which exhibit a diminished ability to meet increased energetic demand. Together, these data
673 indicate that ATF4 drives both metabolic reprogramming and mitochondrial bioenergetic capacity
674 in primary mouse myotubes.
675
676 ***ATF4 regulates cellular redox state and reactive oxygen species (ROS) production***
677 We next sought to understand the functional implications of altered mitochondrial energetics with
678 ATF4 expression by measuring intracellular ROS levels. We observed an increase in ROS buildup
679 following ATF4 deletion, consistent with altered calcium homeostasis and reduced mitochondrial
680 activity (Figure 7J). On the other hand, ATF4 overexpression kept ROS levels stable or slightly
681 decreased them even though mitochondrial respiration increased (Figure 7 H-J), indicating that
682 ATF4 limits oxidative stress by coordinating mitochondrial expansion with redox regulatory
683 systems.
684
685 ***ATF4-dependent metabolic remodeling is supported by transcriptional changes***
686 We utilized targeted qPCR analysis (Figure 7a–o) to examine whether metabolic and functional
687 alterations were occurring with alterations in mitochondrial and metabolic gene transcription
688 levels. Overexpression of ATF4 increased expression of genes regulating mitochondrial
689 metabolism, stress adaptation, and redox homeostasis, whereas ATF4 deletion reduced their
690 expression. These results from metabolomic and bioenergetic studies corroborate the idea that
691 ATF4 regulates metabolic pathways by transcriptional control to facilitate mitochondrial growth,
692 improve respiration, and maintain redox equilibrium. Collectively, our data indicate that loss of
693 ATF4 leads to metabolic dysregulation, reduced respiration, and elevated oxidative stress, whereas
694 ATF4 overexpression causes metabolic reprogramming, improves mitochondrial respiratory
695 capacity, and preserves redox balance.
696 **Induced stress increases ATF4 expression and MERC tethering in human and mouse**
697 **myotube**

698 To gain deeper insight into ATF4 induction during cellular stress, we utilized oligomycin, an
699 inhibitor of mitochondrial ATP synthase, to induce cellular stress in primary human and mouse
700 myotubes. Western blot analysis showed that ATF4 protein expression levels increased with time
701 in primary mouse (Figure 8A) and primary human (Figure 8 B) myotubes. Quantifications of these
702 changes and the protein level changes in MERC tethering machinery (Figure 8 D-H) with induced

703 cellular stress indicate mitochondrial-organelle communication responses initiate quickly and
704 remain elevated with prolonged oligomycin-induced cellular stress.
705
706 ***TEM analysis reveals increased Megamitochondria formation and MERC tethering with***
707 ***oligomycin induced cellular stress***
708 To assess if the increases in ATF4 and MERC tethering machinery protein expression occur
709 concomitantly with the formation of Megamitochondria, we utilized TEM imaging of primary
710 mouse and human myotubes (Figure 8 I-T). We found that prolonged treatment with oligomycin
711 significantly decreased mitochondrial number while simultaneously increasing mitochondrial area
712 in human (Figure 8 I-I", L-N) and mouse (Figure 8 O-O", R-T) primary myotubes. We also found
713 significant decreases in MERC distance after 8-hours of oligomycin treatment (Figure 8 I-I", J, K,
714 O-O", P, Q) with significant increases in MERC length, indicating increased tethering and
715 communication in both human (Figure 8 I-I", J, K) and mouse (Figure 8 O-O", P, Q) primary
716 myotubes. These data collectively indicate that inducing cellular stress with oligomycin treatment
717 produces results in human and mouse myotubes that are consistent with our ATF4 overexpression
718 model.
719

720 **ATF4-driven mitochondrial remodeling is dependent on MFN2 in myotubes**

721 Since mitochondrial morphology is driven and determined by mitochondrial dynamic, we want to
722 determine if the ATF4-induced mitochondrial remodeling we observe is dependent on
723 mitochondrial dynamics machinery. To investigate this, we first measured the abundance of
724 proteins involved in mitochondrial dynamics in ATF4 OE cells. Western blot analysis revealed
725 that with ATF4 overexpression, MFN2 is the only mitochonchondrial dynamics protein that is
726 significantly increased (Figure 9 A-H).

727 ***ATF4-induced mitochondrial network expansion is sensitive to MFN2 inhibition***
728 To determine whether MFN2 was required for the mitochondrial changes observed with ATF4 OE,
729 we used a chemical inhibitor of mitochondrial oligomerization, FMI8. Using spinning disc
730 confocal microscopy, we observed significant changes in MFI8-treated primary myoblasts, both
731 with and without ATF4 overexpression (Figure 9I). The results show that ATF4 OE-induced
732 requires functional MFN2-mediated fusion.

733 Consistent with our other data, quantifications of mitochondrial parameters in our live-cell imaging
734 experiments reveal increases in mitochondrial area and volume and decreased mitochondrial
735 sphericity with ATF4 OE (Figure 9 J, L). Notably, although the addition of MFI8 with ATF4 OE
736 shows significant increases in both mitochondrial area and volume and significant decreases in
737 mitochondrial sphericity in comparison to MFI8 treated GFP control, both groups showed
738 significant mitochondrial fragmentation (Figure 9 K, M).
739
740 ***MFN2 inhibition uncouples ATF4 signaling from mitochondrial expansion***
741 Collectively, these results show that ATF4 overexpression stimulates mitochondrial network
742 growth via a process that depends on fusion and involves MFN2. The fact that ATF4-induced
743 mitochondrial remodeling can be blocked by pharmacological suppression of MFN2
744 oligomerization even when ATF4 expression is sustained suggests that MFN2 is located
745 downstream of ATF4 in the pathway that regulates mitochondrial architecture. Concentric circle
746 analysis revealed that suppression of MFN2 oligomerization prevents the mitochondrial
747 redistribution observed with ATF4 overexpression (Figure 9P, S). According to zone-based
748 quantification, ATF4 whereas blocking MFN2 oligomerization prevents this redistribution. Taken
749 together, these results show that ATF4 transcriptionally programs a coordinated program that leads
750 to increased mitochondrial fusion and elongation. Together, these findings indicate that MFN2 is
751 a crucial effector of ATF4-driven mitochondrial remodeling (Fig. 9 T–U).
752

753 **ATF4 binds to the promotors of NRF1 and Nrf2 during cellular stress to facilitate MFN2-**
754 **dependent mitochondrial remodeling in C2C12 myoblasts**

755 Since it has previously been reported that ATF4 does not bind the promoter of the MFN2 gene, we
756 first confirmed these findings using ChIP-seq in tunicamycin-treated mouse embryonic fibroblasts
757 (MEFs) (Supplemental Figure). Since our findings are consistent with previous reports that ATF4
758 does not bind to the *Mfn2* promoter directly under tunicamycin-induced cellular stress, we then
759 considered other transcription factors known to bind the Mfn2 promoter directly. Interestingly, we
760 found that ATF4 binds to the promoters of the genes encoding NRF1 and Nrf2 during cellular
761 stress, both of which are known to control MFN2 expression (Figure 10 A-B).

762 ***The small molecule inhibitor of Nrf2, Compound 4f, prevents the formation of***
763 ***Megamitochondria typically seen with induced cellular stress***
764 To determine if Nrf2 is required for the ATF4-dependent, MFN2-mediated mitochondrial changes
765 with induced stress, we treated C2C12 myoblasts with either DMSO, thapsigargin, or tunicamycin,
766 with or without the addition of Compound 4f (Figure 10C). We found that, with the addition of 4f,
767 the mitochondrial hyperpolarization typically observed under induced cellular stress is lost (Figure
768 10 D-F), indicating a severe disruption of stress-induced mitochondrial adaptations.
769
770 ***Overexpression of ATF4 with treatment with 4f shows similar results in the loss of***
771 ***Megamitochondria formation seen with induced cellular stress***
772 To determine whether our results observed with induced cellular stress and treatment with 4f could
773 be recapitulated by overexpressing ATF4, we performed identical experiments as in our induced
774 cellular stress model, except that, instead of chemically inducing cellular stress, we used
775 adenovirus expressing either GFP or ATF4 (Figure 10G). As anticipated, the overexpression of
776 ATF4 showed similar changes in mitochondrial morphology and the loss of Megamitochondria
777 formation observed with induced cellular stress (Figure 10G).
778
779 Further quantitative analyses conducted under various experimental settings showed that NRF1
780 and Nrf2 chemical modulation had varied effects on the size, shape, volume, and mass of
781 mitochondria in GFP and ATF4 OE cells (Figure 10 M-R). Specifically, ATF4-driven alterations
782 in mitochondrial size and complexity were downregulated when the NRF pathway was inhibited,
783 suggesting that ATF4 and NRF signaling interact functionally to control mitochondrial structure.
784 Results from Figure 10 show that the NRF1 and Nrf2 signaling pathways play a crucial role in the
785 mitochondrial remodeling induced by ATF4. These results provide support for the idea that ATF4
786 coordinates the redistribution of mitochondrial spatial coordinates and ultrastructural remodeling
787 in response to cellular stress by activating transcriptional programs dependent on NRF1 and Nrf2
788 signaling.
789
790 **Discussion**
791 This study sought to investigate the molecular mechanisms behind mitochondrial and MERC
792 changes observed during cellular stress. We found that ATF4 activation is linked to significant

793 alterations in central carbon metabolism in the *Drosophila* model, including coordinated
794 modifications in tricarboxylic acid cycle intermediates such citrate, fumarate, succinate, and
795 malate. Elevation of these metabolites is consistent with higher anaplerotic flux and mitochondrial
796 metabolic throughput, suggesting that mega-mitochondrial formation and mitochondrial
797 expansion are supported by improved metabolic capacity rather than by bioenergetic collapse. This
798 metabolic state is ideal for maintaining larger mitochondrial volumes, increased cristae surface
799 area, and long-range mitochondrial communication via nanotunneling (Vincent, Turnbull et al.
800 2017, Palese, Rakotobe et al. 2025).
801
802 Importantly, ATF4 activation causes mitochondrial expansion as well as significant modification
803 of cristae architecture. Quantitative ultrastructural analysis reveals that increases in mitochondrial
804 size and volume are accompanied by coordinated changes in cristae number, density, and surface
805 area. These findings show that mega-mitochondria remain bioenergetically structured and
806 functionally competent. As a result, cristae remodeling is a functionally integrated adaptation that
807 supports both the energy requirements of huge mitochondrial networks and elevated oxidative
808 metabolism (Ježek, Jabůrek et al. 2023, Kawano, Bazila et al. 2023).
809
810 Fly metabolomics also reveals changes in amino acid pools, including branched-chain amino acids,
811 methionine, cysteine, and taurine-related metabolites, which directly impact ISR and redox
812 regulatory pathways. These modifications are believed to under stress. Cysteine- and glutathione-
813 related metabolites are particularly significant in connecting ATF4 activation with NRF2-driven
814 antioxidant pathways (Wallis, Morehead et al. 2021). This supports the idea that regulated redox
815 signaling facilitates mitochondrial expansion, cristae remodeling, and fusion. Conversely,
816 excessive oxidative stress would impede these processes.
817 The fly model also affects the MERCS by altering several metabolite types. This metabolic
818 rewiring, driven by ATF4, affects the lipid composition, curvature, and fluidity of the membrane,
819 as reflected by changes in glycerolipid- and phospholipid-related intermediates. As a result of these
820 alterations, larger MERCS should become more stable, allowing for more consistent lipid transfer,
821 coordination of mitochondrial fusion machinery, and prolonged calcium exchange (Szymański,
822 Janikiewicz et al. 2017, Bassot, Chen et al. 2021). Consequently, larger MERCS provide a

biochemical and functional platform that can enable mega-mitochondrial development, cristae alteration, and the generation of Mitochondrial Nanotunnels (Vincent, Turnbull et al. 2017).

Metabolomic analysis shows ATF4 activation in mammalian myotubes. In our in vitro studies, myotubes show alterations in glycolytic intermediates, pyruvate handling, and TCA cycle flux, suggesting metabolically flexible and oxidatively active state (Philp, Perez-Schindler et al. 2010). These changes are consistent with elevated mitochondrial volume and area, modified cristae structure, and enhanced mitochondrial connectivity, indicating that metabolic remodeling actively enlarges mitochondria (Kawano, Bazila et al. 2023).

Metabolic–calcium–redox pathway seems to be very important for controlling mitochondrial nanotunnel formation (Lavorato, Iyer et al. 2017, Vincent, Turnbull et al. 2017). Requirements for the formation of nanotunnels include remodeling the membrane, coordinate the cytoskeleton, and provide constant energy input (Vincent, Turnbull et al. 2017, Lavorato 2018). The metabolic patterns observed in the fly and myotube models are consistent with the biosynthetic and energetic needs fundamental to the formation and maintenance of nanotunnels. As a potential alternative to stress-induced damage, nanotunneling could be an adaptive, ISR-driven method for transporting metabolites, calcium, and redox signals across widely distributed mitochondria (Vincent, Turnbull et al. 2017).

ATF4 activation reshaped mitochondrial spatial organization. Quantitative spatial analysis revealed redistribution across perinuclear, nuclear-adjacent, radial, and distal cytoplasmic zones. ATF4 overexpression promoted mitochondrial enrichment in perinuclear and radial regions, whereas ATF4 knockdown produced fragmented mitochondria confined to the cell periphery. Perinuclear localization promotes sustained interactions with the endoplasmic reticulum and calcium exchange, whereas radial organization along cytoskeletal tracks enables nanotunnel formation that links distant mitochondrial domains (Vincent, Turnbull et al. 2017). This coordinated zonal positioning is therefore essential for long-range mitochondrial communication and network cohesion.

MFN2 controls fusion and MERC tethering, which connects changes in cristae shape, mitochondrial size, and nanotunneling (Vincent, Turnbull et al. 2017, Zaman and Shutt 2022). These structural changes are interconnected, as MFN2 disruption abolishes mitochondrial extension, nanotunneling, and zonal redistribution (Sood 2015, Vincent, Turnbull et al. 2017). Calcium and redox signaling appear to function within this framework to couple metabolic output to membrane dynamics and cytoskeletal interactions required for large-scale mitochondrial remodeling. Comparison of in vivo and in vitro systems highlight how physiological context modulates ATF4-dependent regulation: systemic inputs in vivo broaden metabolic engagement downstream of ATF4, strengthening lipid and redox pathway involvement and promoting sustained mega-mitochondrial formation across tissues. Therefore, ATF4-driven ISR signaling is sufficient to alter mitochondrial size, cristae architecture, spatial organization and connectivity with activation.

Collectively, ATF4 is established as a master regulator that integrates ISR and metabolic state, calcium and redox signaling, and spatial organization to control mitochondrial architecture at several scales. ATF4 establishes ISR regulation as a key factor in determining mitochondrial health in physiology and disease by controlling MERC dynamics and metabolic flux, which determines whether Megamitochondria and mitochondrial nanotunneling serve adaptive stress responses or become maladaptive under chronic or pathological conditions.

Conflict of interest

The authors declare that they have no conflict of interest.

Data availability statement

All data generated or analyzed during this study are included in this published article and its Supplementary information files. Additional data can be requested from the corresponding author.

Acknowledgments

UNCF/Bristol-Myers Squibb E.E. Just Faculty Fund, Career Award at the Scientific Interface (CASI Award) from the Burroughs Welcome Fund (BWF) ID # 1021868.01, BWF Ad-hoc Award, NIH Small Research Pilot Subaward 5R25HL106365-12 from the National Institutes of Health PRIDE Program, DK020593, Vanderbilt Diabetes and Research Training Center for DRTC

Alzheimer's Disease Pilot & Feasibility Program, CZI Science Diversity Leadership grant number 2022-253529 from the Chan Zuckerberg Initiative DAF, an advised fund of the Silicon Valley Community Foundation to A.H.J. NSF NRT grant 19-22697 (to A.C.), NSF BPE grant 22-17621 (to A.C.), and the Asness Family Fund through the Frist Center for Autism & Innovation (K. Stassun, PI) (to A.C.) This work was also supported by National Institutes of Health HL006221 (BG).

Figure and Legends

Figure 1. ATF4 expression alters mitochondrial morphology in *Drosophila* flight muscle. 3D reconstruction of Serial Block Face-Scanning Electron Microscopy (SBF-SEM) images for Wildtype (WT)

(A-A”), ATF4 KD (B-B’”), and ATF4 OE (C-C”). Quantifications of mitochondrial volume between groups in A-C (D). 3D reconstruction using Imaris image analysis software of extracted flight muscle from WT (E), ATF4 KD (F), and ATF4 OE (G) models with GFP labeled mitochondria (E’, F’, and G’, respectively) and actin labeled in red (E”, F”, and G”, respectively). Quantitative comparisons between groups are provided for mitochondrial volume (H), mitochondrial length (I), and mitochondrial sphericity (J). Data was analyzed using an unpaired t-test. When more than two groups were compared, a one-way analysis of variance (ANOVA) was used, and statistical significance was determined by Tukey’s multiple comparisons test. A significant difference is defined as *$p < 0.05$, **$p < 0.01$, ***$p < 0.001$, ****$p < 0.0001$.

Figure 2. ATF4 expression alters mitochondria, MERCS, and gene expression in *Drosophila* flight muscle. TEM imaging shows alterations in WT

(A-A”), ATF4 KO (B-B”), and ATF4 OE (C-C”) mitochondria at different magnifications. Comparative quantifications between groups for cristae surface area (D), cristae number (E), muscle glycogen content as measured by glycogen-area following TEM imaging (F), mitochondrial area (G), mitochondrial circularity index (H), and mitochondrial number (I). Higher magnification TEM image of *Drosophila* flight muscle for WT (J), ATF4 KD (K), and ATF4 OE (L). Comparative quantification between groups for MERC length (M) and MERC distance (N). O) Representative schematic image showing the orientation of measurement for MERC distance

914 and length. Confocal imaging of flight muscle from WT and ATF4 OE with actin labeled red (P
915 and Q, respectively), HA labeled mitochondria (green) (P' and Q', respectively), DAPI stained
916 nuclei (P" and Q", respectively), and overlaid (P"' and Q"', respectively). Confocal (R) and TEM
917 (R") imaging of mitochondrial nanotunneling observed in ATF4 OE flight muscle as indicated by
918 arrows. 3D reconstructions with orthoslice of nanotunnels in *Drosophila* flight muscle from SBF-
919 SEM imaging for WT (S-S"), ATF4 OE (T-T"), and ATF4 KD (U-U"). TEM quantifications of
920 Megamitochondria (V) and nanotunnel frequency (W) in control group, ATF4 OE, and ATF4 KD
921 tissue. SBF-SEM datasets showing nanotunnels, mitochondrial volume and mega mitochondrial
922 volume in control group, ATF4 OE, and ATF4 KD tissue. (a), mitochondrial dynamics (b), Ca^{2+}
923 signaling (c), and Ca^{2+} transport (d). Data was analyzed using an unpaired t test. When more than
924 two groups were compared, a one-way analysis of variance (ANOVA) was used, and statistical
925 significance was determined by Tukey's multiple comparisons test. A significant difference is
926 defined as *$p < 0.05$, **$p < 0.01$, ***$p < 0.001$, ****$p < 0.0001$.
927

928 **Figure 3. ATF4 expression modulates mitochondrial morphology in murine myotubes.**

929 Primary mouse myotubes were transduced with adenovirus expressing GFP (A), GFP-cre (B), or
930 ATF4 OE (C) adenovirus. TEM imaging of control (D), ATF4 KO (E), ATF4 OE 24-hours post-
931 infections (F), and ATF4 OE 48-hours post-infection (G). Comparative quantifications of
932 mitochondrial area (H), cristae score (I), and MERC distance (J) between groups. Metabolomic
933 profiling core metabolic pathways in IFM (K). Data was analyzed using an unpaired t test. When
934 more than two groups were compared, a one-way analysis of variance (ANOVA) was used, and
935 statistical significance was determined by Tukey's multiple comparisons test. A significant
936 difference is defined as *$p < 0.05$, **$p < 0.01$, ***$p < 0.001$, ****$p < 0.0001$.

937 **Figure 4. ATF4 regulates mitochondrial ultrastructure and calcium handling in myotubes**
938 (A–C) Representative fluorescence images of myotubes infected with either adenovirus expressing
939 GFP or ATF4. The presence of fluorescence indicates successful infection. Scale bar, 10X. (D–G)
940 Transmission electron microscopy (TEM) images of myotubes reveal ultrastructural mitochondrial
941 remodeling associated with ATF4 expression. Control myotubes exhibit elongated mitochondria
942 with well-organized cristae aligned along the contractile axis. In contrast, ATF4 manipulation
943 results in altered mitochondrial size, shape, and cristae organization, with increased mitochondrial

944 heterogeneity and disruption of longitudinal alignment. Blue arrows indicate representative
945 mitochondria. Scale bar, 2 μm. (H–J) Quantification of mitochondrial ultrastructural parameters
946 in myotubes, including mitochondrial area, aspect ratio, and cristae density. ATF4 overexpression
947 (OE) and ATF4 knockout (KO) differentially regulate mitochondrial morphology, consistent with
948 distinct effects on mitochondrial fusion–fission balance and internal membrane organization. Data
949 are presented as mean ± SEM. (K) Representative cytosolic calcium traces measured by Fura-2
950 AM (340/380 nm) in myotubes following stimulation. Control myotubes display robust and
951 sustained calcium transients, whereas ATF4 KO and ATF4 OE myotubes exhibit blunted calcium
952 responses, indicating impaired calcium handling. (L) Quantification of peak calcium amplitude
953 reveals a significant reduction in calcium signaling in ATF4 KO and ATF4 OE myotubes
954 compared with controls. ****$P < 0.0001$. (M) Area under the curve (AUC) analysis of calcium
955 transients demonstrates reduced overall calcium signaling in ATF4 KO myotubes compared with
956 controls, whereas ATF4 OE shows no significant difference relative to control. **$P < 0.01$; ns, not
957 significant.

958 **Figure 5. ATF4 regulates mitochondrial–ER contact architecture and mitochondrial network**
959 **organization in myotubes and myoblasts**

960 (A–C) Representative serial block-face scanning electron microscopy (SBF-SEM) images of
961 myotubes showing mitochondrial–ER contact sites (MERCS; cyan) overlaid on ultrastructural
962 images under Control, ATF4 knockout (KO), and ATF4 overexpression (OE) conditions. (A′–C′)
963 Three-dimensional reconstructions of MERCS segmented from SBF-SEM datasets corresponding
964 to panels A–C, illustrating ATF4-dependent changes in MERC size, continuity, and spatial
965 organization. (D) Quantification of total MERC volume (nm^3) per myotube demonstrates a
966 significant increase in MERC volume with ATF4 OE and a marked reduction with ATF4 KO
967 compared with Control. (E) Quantification of total 3D MERC length (nm) per myotube confirms
968 ATF4-dependent enhancement of ER–mitochondria contact length, with ATF4 OE showing
969 increased MERC length and ATF4 KO showing reduced contacts. (F–G) Representative
970 transmission electron microscopy (TEM) images of myotubes highlighting longitudinal
971 mitochondrial alignment and ER–mitochondria interfaces in Control and ATF4 OE conditions. (H–
972 I) Pseudocolored segmentation of mitochondria from TEM images in panels F–G, illustrating
973 increased mitochondrial elongation and network complexity in ATF4 OE myotubes. (J–K) Three-
974 dimensional reconstructions of mitochondrial networks in myotubes reveal increased

975 mitochondrial volume and connectivity in ATF4 OE relative to Control. (L) Quantification of total
976 mitochondrial volume (nm^3) in myotubes shows a significant increase in mitochondrial volume
977 with ATF4 OE compared with ATF4-deficient myotubes. (M–N) Representative stimulated
978 emission depletion (STED) microscopy images of C2C12 myotubes stained for mitochondria (red)
979 and nuclei (blue), demonstrating altered mitochondrial network density and perinuclear
980 organization under ATF4 manipulation. (P) Spinning disk confocal images of control primary
981 myoblasts expressing GFP and stained with MitoTracker. (P) GFP (green) marks the cell body;
982 (P′) MitoTracker (red) labels the mitochondrial network; (P″) merged image illustrates
983 mitochondrial distribution relative to cell morphology. (Q) Spinning disk confocal images of ATF4
984 OE myoblasts expressing GFP and stained with MitoTracker. (Q) GFP (green); (Q′) MitoTracker
985 (red); (Q″) merged image reveals increased mitochondrial network density and elongation in ATF4
986 OE primary mouse myoblasts compared with control.

987 **Figure 6. ATF4 expression alters genes associated with mitochondria and MERCs in**
988 ***Drosophila* flight muscle.**

989 A) RNA sequencing data from ATF4 KD showing differentially expressed genes. B) Volcano plot
990 of p-adjusted RNA sequencing data shown in (A). C) RNA sequencing data from ATF4 OE
991 showing differentially expressed genes. D) Volcano plot of p-adjusted RNA sequencing data shown
992 in (C). E) Changes in canonical pathways from RNA sequencing data from ATF4 KD and OE. F)
993 Differentially expressed upstream regulators from RNA sequencing data from ATF4 KD and OE.
994 G) Gene set enrichment analysis (GSEA) for biological processes in ATF4 KD and OE flight
995 muscle. H)

996 **Figure 7. ATF4 overexpression alters mitochondrial function and gene expression levels.**

997 A) Principal component analysis (PCA) score plot based on primary mouse myotubes of Control,
998 ATF4 KO, and ATF4 OE models (n = 3). B) Bubble plot of fold change abundance of metabolic
999 species in Control (Red) and ATF4 KO (Green) primary mouse myotubes. C) Differential heatmap
1000 from metabolomic data for control, ATF4 KO, and ATF4 OE primary mouse myotubes. H)
1001 Enrichment analysis from the obtained metabolomic data obtained from each group from primary
1002 mouse myotubes. I) Oxygen consumption rate (OCR) measurements from each group.
1003 Comparative quantifications for maximum OCR (J), spare capacity (K), basal OCR (L), ATP-
1004 linked OCR (M), and mitochondrial H2O2 content (N) between groups measured by mitochondrial

1005 peroxy yellow 1 (MitoPY1). Relative gene expression levels between groups for FGF21 (a),
1006 TFAM (b), PPARGc1 (c), PGC1 alpha (d), ATF3 (e), BIP (f), PERK (g), CHOP (h), ATF5 (i),
1007 sXBP1 (j), NRF2 (k), ERO1α (l) GADD34 (m), GRP75 (n) VDAC3 (o) from primary mouse
1008 myotubes. Data was analyzed using an unpaired t-test. When more than two groups were
1009 compared, a one-way analysis of variance (ANOVA) was used, and statistical significance was
1010 determined by Tukey's multiple comparisons test. A significant difference is defined as *$p < 0.05$,
1011 **$p < 0.01$, ***$p < 0.001$, ****$p < 0.0001$.

1012 **Figure 8. Induced stress increases ATF4 expression and MERC tethering.**

1013 Relative gene expression of ATF4 following oligomycin treatment for 0-hour, 30-minute and 8-
1014 hour in primary mouse (A) and primary human (B) myotubes. C) Representative Western blot and
1015 quantifications for ATF4 (D) and MERC tethering proteins: GRP75 (E), IP3R3 (F), VDAC (G),
1016 and BIP (H) following oligomycin treatment in primary mouse myotubes. I) TEM imaging of
1017 human primary myotubes treated with Oligomycin for 0-minutes, 30-minutes (I'), and 8-hours
1018 (I"). Quantitative comparisons for MERC distance (J), MERC length (K), mitochondrial number
1019 (L), mitochondrial circularity index (M), and mitochondrial area (N) changes between groups
1020 shown in I-I" following Oligomycin treatment. TEM imaging of primary mouse myotubes treated
1021 with Oligomycin for 0-minutes (O), 30-minutes (O'), and 8-hours (O"). Quantitative comparison
1022 of MERC distance (P), MERC length (Q), mitochondrial number (R), mitochondrial circularity
1023 index (S), and mitochondrial area (T) changes in primary mouse myotubes following—
1024 Oligomycin—Oligomycin treatment. Data was analyzed using an unpaired t test. When more than
1025 two groups were compared, a one-way analysis of variance (ANOVA) was used, and statistical
1026 significance was determined by Tukey's multiple comparisons test. A significant difference is
1027 defined as *$p < 0.05$, **$p < 0.01$, ***$p < 0.001$, ****$p < 0.0001$.

1028 **Figure 9. Expression levels for proteins involved in mitochondrial dynamics change with**
1029 **ATF4 expression.**

1030 A) Representative Western blots from control and ATF4 OE primary myotubes showing
1031 mitochondrial dynamic proteins. Comparative quantifications of protein levels for MFN2 (B),
1032 MFN1 (C), ATF4 (D), DRP1 (E), and OPA1 (F). Comparison of relative gene expression levels
1033 for MFN2 (G) and MFN1 (H) in primary mouse myotubes between Control, ATF4 KO, and ATF4
1034 OE. I) Representative confocal microscopy images revealing mitochondrial morphology for GFP

1035 Control or ATF4 OE cells treated with dimethyl sulfoxide (DMSO) or the MFN2 oligomerization
1036 inhibitor, MFI8. J, K) Mitochondrial area (J) and aspect ratio (K) intensity analyses under basal
1037 conditions for DMSO or MFI8 treatments, demonstrating that ATF4 OE increases mitochondrial
1038 size and elongation through MFN2. L–O) Histograms for mitochondrial area (L, M) and aspect
1039 ratio (N, O) comparing Control versus ATF4 OE cells. P) Analysis of mitochondrial network
1040 features under all experimental conditions. Q, R) Percentage of total network versus separates
1041 mitochondria for Control and ATF4 OE cells. S) Mitochondrial network measures for all treatment
1042 groups. T, U) Additional mitochondrial morphology studies under Control versus ATF4 OE
1043 conditions. Data represent mean ± SEM. *P < 0.05, **P < 0.01, ***P < 0.001, ****P < 0.0001.

1044 **Figure 10. Chromatin immunoprecipitation sequencing (ChIP-Seq) analysis from WT and**
1045 **ATF4 or CHOP deficient MEFs treated with tunicamycin.**

1046 ATF4 and CHOP bind to promotors of the genes encoding NRF1 (A) and Nrf2 (B) during cellular
1047 stress. (C) Representative confocal microscopy images showing mitochondrial distribution
1048 (MitoView650, red) and nuclei (DAPI, blue) for C2C12 myoblasts under basal conditions or
1049 treated with "Compound 4f," a small molecule inhibitor of Nrf2 (D-F). Representative confocal
1050 images showing mitochondrial morphology (MitoView650, red) in myoblasts from controls and
1051 ATF4-overexpressing (ATF4 OE) cultures treated with either DMSO (vehicle) or Compound 4f
1052 (G). Analysis of mitochondrial properties in controls compared with ATF4 OE cells under
1053 pharmacological treatment (H–L): mitochondrial area (H), mitochondrial width (I), mitochondrial
1054 aspect ratio (J), mitochondrial volume (K), mitochondrial sphericity (L). The red bar represents
1055 increased mitochondrial properties compared with controls. C2C12 myoblasts were infected with
1056 adenovirus expressing GFP or ATF4 with and without the presence of inhibitors of NRF2, Nrf2,
1057 or the combination of both. (M–R). Mitochondrial density (arbitrary units) was analyzed as the
1058 integrated fluorescence intensity normalized to myotube area in GFP control, NRF1, and NRF2-
1059 overexpressing cells (M) and in ATF4 OE cells (N). Mitochondrial area (μm2) was measured as
1060 the mean area of mitochondrial structures in GFP, NRF1, NRF2 cells (O) and ATF4 OE cells (P).
1061 Mitochondrial aspect ration (μ2) was measured in GFP, NRF1, NRF2 cells (Q) and ATF4 OE cells
1062 (R).

1063

1064

References

Adams, C. M., S. M. Ebert and M. C. Dyle (2017). "Role of ATF4 in skeletal muscle atrophy." Curr Opin Clin Nutr Metab Care **20**(3): 164–168.

Bartsakoulia, M., A. Pyle, D. Troncoso-Chandía, J. Vial-Brizzi, M. V. Paz-Fiblas, J. Duff, H. Griffin, V. Boczonadi, H. Lochmüller, S. Kleinle, P. F. Chinnery, S. Grünert, J. Kirschner, V. Eisner and R. Horvath (2018). "A novel mechanism causing imbalance of mitochondrial fusion and fission in human myopathies." Hum Mol Genet **27**(7): 1186–1195.

Bassot, A., J. Chen and T. Simmen (2021). "Post-translational modification of cysteines: a key determinant of endoplasmic reticulum-mitochondria contacts (MERCs)." Contact **4**: 25152564211001213.

Boudina, S., S. Sena, H. Theobald, X. Sheng, J. J. Wright, X. X. Hu, S. Aziz, J. I. Johnson, H. Bugger, V. G. Zaha and E. D. Abel (2007). "Mitochondrial energetics in the heart in obesity-related diabetes: direct evidence for increased uncoupled respiration and activation of uncoupling proteins." Diabetes **56**(10): 2457–2466.

Bratic, A. and N. G. Larsson (2013). "The role of mitochondria in aging." J Clin Invest **123**(3): 951–957.

Bustos, G., P. Cruz, A. Lovy and C. Cárdenas (2017). "Endoplasmic Reticulum-Mitochondria Calcium Communication and the Regulation of Mitochondrial Metabolism in Cancer: A Novel Potential Target." Front Oncol **7**: 199.

Chan, D. C. (2012). "Fusion and fission: interlinked processes critical for mitochondrial health." Annu Rev Genet **46**: 265–287.

Cogliati, S., J. A. Enriquez and L. Scorrano (2016). "Mitochondrial Cristae: Where Beauty Meets Functionality." Trends Biochem Sci **41**(3): 261–273.

Del Campo, A., I. Contreras-Hernández, M. Castro-Sepúlveda, C. A. Campos, R. Figueroa, M. F. Tevy, V. Eisner, M. Casas and E. Jaimovich (2018). "Muscle function decline and mitochondria changes in middle age precede sarcopenia in mice." Aging (Albany NY) **10**(1): 34–55.

Dong, Z. and X. Yao (2022). "Insight of the role of mitochondrial calcium homeostasis in hepatic insulin resistance." Mitochondrion **62**: 128–138.

Ebert, S. M., M. C. Dyle, S. D. Kunkel, S. A. Bullard, K. S. Bongers, D. K. Fox, J. M. Dierdorff, E. D. Foster and C. M. Adams (2012). "Stress-induced skeletal muscle Gadd45a expression reprograms myonuclei and causes muscle atrophy." J Biol Chem **287**(33): 27290–27301.

Garza-Lopez, E., Z. Vue, P. Katti, K. Neikirk, M. Biete, J. Lam, H. K. Beasley, A. G. Marshall, T. A. Rodman, T. A. Christensen, J. L. Salisbury, L. Vang, M. Mungai, S. AshShareef, S. A. Murray,

J. Shao, J. Streeter, B. Glancy, R. O. Pereira, E. D. Abel and A. Hinton, Jr. (2021). "Protocols for Generating Surfaces and Measuring 3D Organelle Morphology Using Amira." Cells **11**(1).

Glancy, B. (2020). "Visualizing Mitochondrial Form and Function within the Cell." Trends Mol Med **26**(1): 58–70.

Hall, H., P. Medina, D. A. Cooper, S. E. Escobedo, J. Rounds, K. J. Brennan, C. Vincent, P. Miura, R. Doerge and V. M. Weake (2017). "Transcriptome profiling of aging Drosophila photoreceptors reveals gene expression trends that correlate with visual senescence." BMC Genomics **18**(1): 894.

Han, J., S. H. Back, J. Hur, Y. H. Lin, R. Gildersleeve, J. Shan, C. L. Yuan, D. Krokowski, S. Wang, M. Hatzoglou, M. S. Kilberg, M. A. Sartor and R. J. Kaufman (2013). "ER-stress-induced transcriptional regulation increases protein synthesis leading to cell death." Nat Cell Biol **15**(5): 481–490.

Hara, Y., F. Yuk, R. Puri, W. G. Janssen, P. R. Rapp and J. H. Morrison (2014). "Presynaptic mitochondrial morphology in monkey prefrontal cortex correlates with working memory and is improved with estrogen treatment." Proc Natl Acad Sci U S A **111**(1): 486–491.

Hinton, A., Jr., S. M. Claypool, K. Neikirk, N. Senoo, C. N. Wanjalla, A. Kirabo and C. R. Williams (2024). "Mitochondrial Structure and Function in Human Heart Failure." Circ Res **135**(2): 372–396.

Hinton, A., Jr., P. Katti, T. A. Christensen, M. Mungai, J. Shao, L. Zhang, S. Trushin, A. Alghanem, A. Jaspersen, R. E. Geroux, K. Neikirk, M. Biete, E. G. Lopez, B. Shao, Z. Vue, L. Vang, H. K. Beasley, A. G. Marshall, D. Stephens, S. Damo, J. Ponce, C. K. E. Bleck, I. Hicsasmaz, S. A. Murray, R. A. C. Edmonds, A. Dajles, Y. D. Koo, S. Bacevac, J. L. Salisbury, R. O. Pereira, B. Glancy, E. Trushina and E. D. Abel (2023). "A Comprehensive Approach to Sample Preparation for Electron Microscopy and the Assessment of Mitochondrial Morphology in Tissue and Cultured Cells." Adv Biol (Weinh) **7**(10): e2200202.

Hinton, A., Jr., P. Katti, M. Mungai, D. D. Hall, O. Koval, J. Shao, Z. Vue, E. G. Lopez, R. Rostami, K. Neikirk, J. Ponce, J. Streeter, B. Schickling, S. Bacevac, C. Grueter, A. Marshall, H. K. Beasley, Y. Do Koo, S. C. Bodine, N. G. R. Nava, A. M. Quintana, L. S. Song, I. M. Grumbach, R. O. Pereira, B. Glancy and E. D. Abel (2024). "ATF4-dependent increase in mitochondrial-endoplasmic reticulum tethering following OPA1 deletion in skeletal muscle." J Cell Physiol **239**(4): e31204.

Jenkins, B. C., K. Neikirk, P. Katti, S. M. Claypool, A. Kirabo, M. R. McReynolds and A. Hinton, Jr. (2024). "Mitochondria in disease: changes in shapes and dynamics." Trends Biochem Sci **49**(4): 346–360.

Ježek, P., M. Jabůrek, B. Holendová, H. Engstová and A. Dlasková (2023). "Mitochondrial cristae morphology reflecting metabolism, superoxide formation, redox homeostasis, and pathology." Antioxidants & Redox Signaling **39**(10-12): 635–683.

Katti, P., M. Rai, S. Srivastava, P. D'Silva and U. Nongthomba (2021). "Marf-mediated mitochondrial fusion is imperative for the development and functioning of indirect flight muscles (IFMs) in drosophila." Exp Cell Res **399**(2): 112486.

Kawano, I., B. Bazila, P. Ježek and A. Dlasková (2023). "Mitochondrial dynamics and cristae shape changes during metabolic reprogramming." Antioxidants & Redox Signaling **39**(10-12): 684–707.

Lam, J., P. Katti, M. Biete, M. Mungai, S. AshShareef, K. Neikirk, E. Garza Lopez, Z. Vue, T. A. Christensen, H. K. Beasley, T. A. Rodman, S. A. Murray, J. L. Salisbury, B. Glancy, J. Shao, R. O. Pereira, E. D. Abel and A. Hinton, Jr. (2021). "A Universal Approach to Analyzing Transmission Electron Microscopy with ImageJ." Cells **10**(9).

Lavorato, M. (2018). "Microtubules and mitochondria nanotunnels." Physiological Mini Reviews **11**.

Lavorato, M., V. R. Iyer, W. Dewight, R. R. Cupo, V. Debattisti, L. Gomez, S. De la Fuente, Y.-T. Zhao, H. H. Valdivia and G. Hajnóczky (2017). "Increased mitochondrial nanotunneling activity, induced by calcium imbalance, affects intermitochondrial matrix exchanges." Proceedings of the National Academy of Sciences **114**(5): E849–E858.

Mustafi, D., S. Kikano and K. Palczewski (2014). "Serial block face-scanning electron microscopy: a method to study retinal degenerative phenotypes." Curr Protoc Mouse Biol **4**(4): 197–204.

Neikirk, K., E. G. Lopez, A. G. Marshall, A. Alghanem, E. Krystofiak, B. Kula, N. Smith, J. Shao, P. Katti and A. Hinton, Jr. (2023). "Call to action to properly utilize electron microscopy to measure organelles to monitor disease." Eur J Cell Biol **102**(4): 151365.

Pakos-Zebrucka, K., I. Koryga, K. Mnich, M. Ljujic, A. Samali and A. M. Gorman (2016). "The integrated stress response." EMBO Rep **17**(10): 1374–1395.

Palese, F., M. Rakotobe and C. Zurzolo (2025). "Transforming the concept of connectivity: unveiling tunneling nanotube biology and their roles in brain development and neurodegeneration." Physiological Reviews **105**(3): 1823–1865.

Patra, A. K., Y. M. Kwon, S. G. Kang, Y. Fujiwara and S. J. Kim (2016). "The complete mitochondrial genome sequence of the tubeworm Lamellibrachia satsuma and structural conservation in the mitochondrial genome control regions of Order Sabellida." Mar Genomics **26**: 63–71.

Pereira, R. O., S. M. Tadinada, F. M. Zasadny, K. J. Oliveira, K. M. P. Pires, A. Olvera, J. Jeffers, R. Souvenir, R. McGlauflin, A. Seei, T. Funari, H. Sesaki, M. J. Potthoff, C. M. Adams, E. J. Anderson and E. D. Abel (2017). "OPA1 deficiency promotes secretion of FGF21 from muscle that prevents obesity and insulin resistance." Embo j **36**(14): 2126–2145.

Philp, A., J. Perez-Schindler, C. Green, D. L. Hamilton and K. Baar (2010). "Pyruvate suppresses PGC1α expression and substrate utilization despite increased respiratory chain content in C2C12 myotubes." American Journal of Physiology-Cell Physiology **299**(2): C240–C250.

Rasmussen, B. B. and C. M. Adams (2020). "ATF4 is a fundamental regulator of nutrient sensing and protein turnover." The Journal of Nutrition **150**(5): 979–980.

Schneider, C. A., W. S. Rasband and K. W. Eliceiri (2012). "NIH Image to ImageJ: 25 years of image analysis." Nat Methods **9**(7): 671–675.

Sood, A. (2015). "Wiring the adaptive response of mitochondria to metabolic transitions: a Mitofusin-2-dependent proteolytic elimination of OPA1 accompanies cristae and mitochondria-ER contacts remodelling in the postprandial mouse liver."

Szymański, J., J. Janikiewicz, B. Michalska, P. Patalas-Krawczyk, M. Perrone, W. Ziółkowski, J. Duszyński, P. Pinton, A. Dobrzyń and M. R. Więckowski (2017). "Interaction of mitochondria with the endoplasmic reticulum and plasma membrane in calcium homeostasis, lipid

trafficking and mitochondrial structure." International Journal of Molecular Sciences **18**(7): 1576.

Tameire, F., Verginadis, II, N. M. Leli, C. Polte, C. S. Conn, R. Ojha, C. Salas Salinas, F. Chinga, A. M. Monroy, W. Fu, P. Wang, A. Kossenkov, J. Ye, R. K. Amaravadi, Z. Ignatova, S. Y. Fuchs, J. A. Diehl, D. Ruggero and C. Koumenis (2019). "ATF4 couples MYC-dependent translational activity to bioenergetic demands during tumour progression." Nat Cell Biol **21**(7): 889–899.

Vincent, A. E., D. M. Turnbull, V. Eisner, G. Hajnóczky and M. Picard (2017). "Mitochondrial nanotunnels." Trends in cell biology **27**(11): 787–799.

Vue, Z., K. Neikirk, L. Vang, E. Garza-Lopez, T. A. Christensen, J. Shao, J. Lam, H. K. Beasley, A. G. Marshall, A. Crabtree, J. Anudokem, Jr., B. Rodriguez, B. Kirk, S. Bacevac, T. Barongan, B. Shao, D. C. Stephens, K. Kabugi, H. J. Koh, A. Koh, C. S. Evans, B. Taylor, A. K. Reddy, T. Miller-Fleming, K. V. Actkins, E. Zaganjor, N. Daneshgar, S. A. Murray, B. C. Mobley, S. M. Damo, J. A. Gaddy, B. Riggs, C. Wanjalla, A. Kirabo, M. McReynolds, J. A. Gomez, M. A. Phillips, V. Exil, D. F. Dai and A. Hinton, Jr. (2023). "Three-dimensional mitochondria reconstructions of murine cardiac muscle changes in size across aging." Am J Physiol Heart Circ Physiol **325**(5): H965–h982.

Wallis, K. F., L. C. Morehead, J. T. Bird, S. D. Byrum and I. R. Miousse (2021). "Differences in cell death in methionine versus cysteine depletion." Environmental and molecular mutagenesis **62**(3): 216–226.

Wende, A. R., B. T. O'Neill, H. Bugger, C. Riehle, J. Tuinei, J. Buchanan, K. Tsushima, L. Wang, P. Caro, A. Guo, C. Sloan, B. J. Kim, X. Wang, R. O. Pereira, M. A. McCrory, B. G. Nye, G. A. Benavides, V. M. Darley-Usmar, T. Shioi, B. C. Weimer and E. D. Abel (2015). "Enhanced cardiac Akt/protein kinase B signaling contributes to pathological cardiac hypertrophy in part by impairing mitochondrial function via transcriptional repression of mitochondrion-targeted nuclear genes." Mol Cell Biol **35**(5): 831–846.

Zaman, M. and T. E. Shutt (2022). "The role of impaired mitochondrial dynamics in MFN2-mediated pathology." Frontiers in cell and developmental biology **10**: 858286.

Zou, Z., T. Ohta, F. Miura and S. Oki (2022). "ChIP-Atlas 2021 update: a data-mining suite for exploring epigenomic landscapes by fully integrating ChIP-seq, ATAC-seq and Bisulfite-seq data." Nucleic Acids Res **50**(W1): W175–w182.

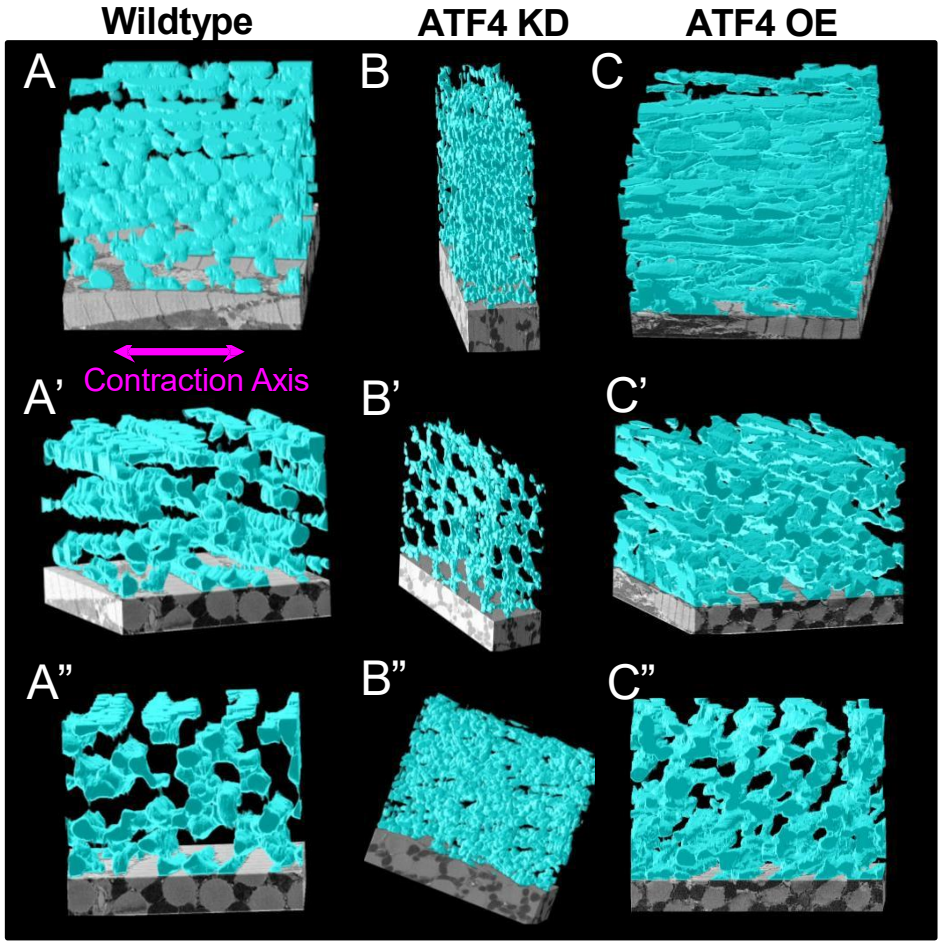
Wildtype
ATF4 KD
ATF4 OE
A
B
C
Contraction Axis
A'
B'
C'
A"
B"
C"

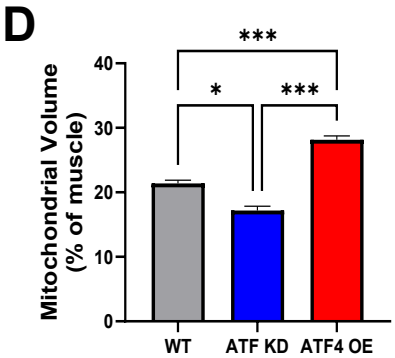
D
Mitochondrial Volume (% of muscle)
40
30
20
10
0
***
*
***
WT
ATF KD
ATF4 OE

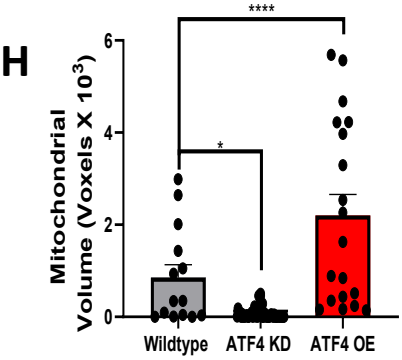
H
Mitochondrial Volume (Voxels X 10³)
6
4
2
0
****
*
Wildtype
ATF4 KD
ATF4 OE

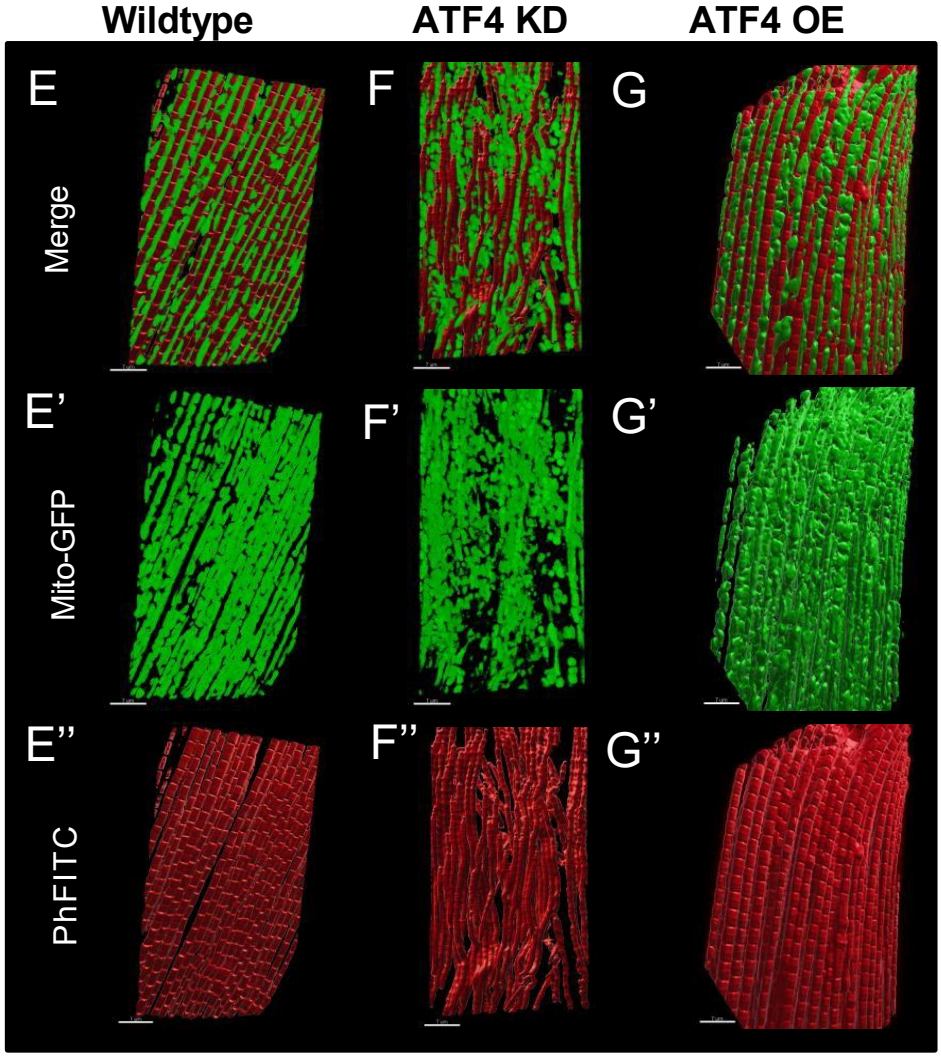
Wildtype
ATF4 KD
ATF4 OE
E
F
G
Merge
E'
F'
G'
Mito-GFP
E"
F"
G"
PhFITC

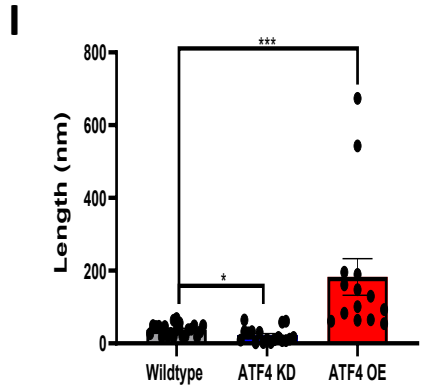
I
Length (nm)
800
600
400
200
0
***
*
Wildtype
ATF4 KD
ATF4 OE

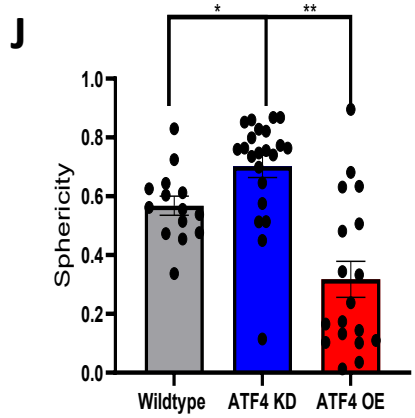
J
Sphericity
1.0
0.8
0.6
0.4
0.2
0.0
*
**
Wildtype
ATF4 KD
ATF4 OE

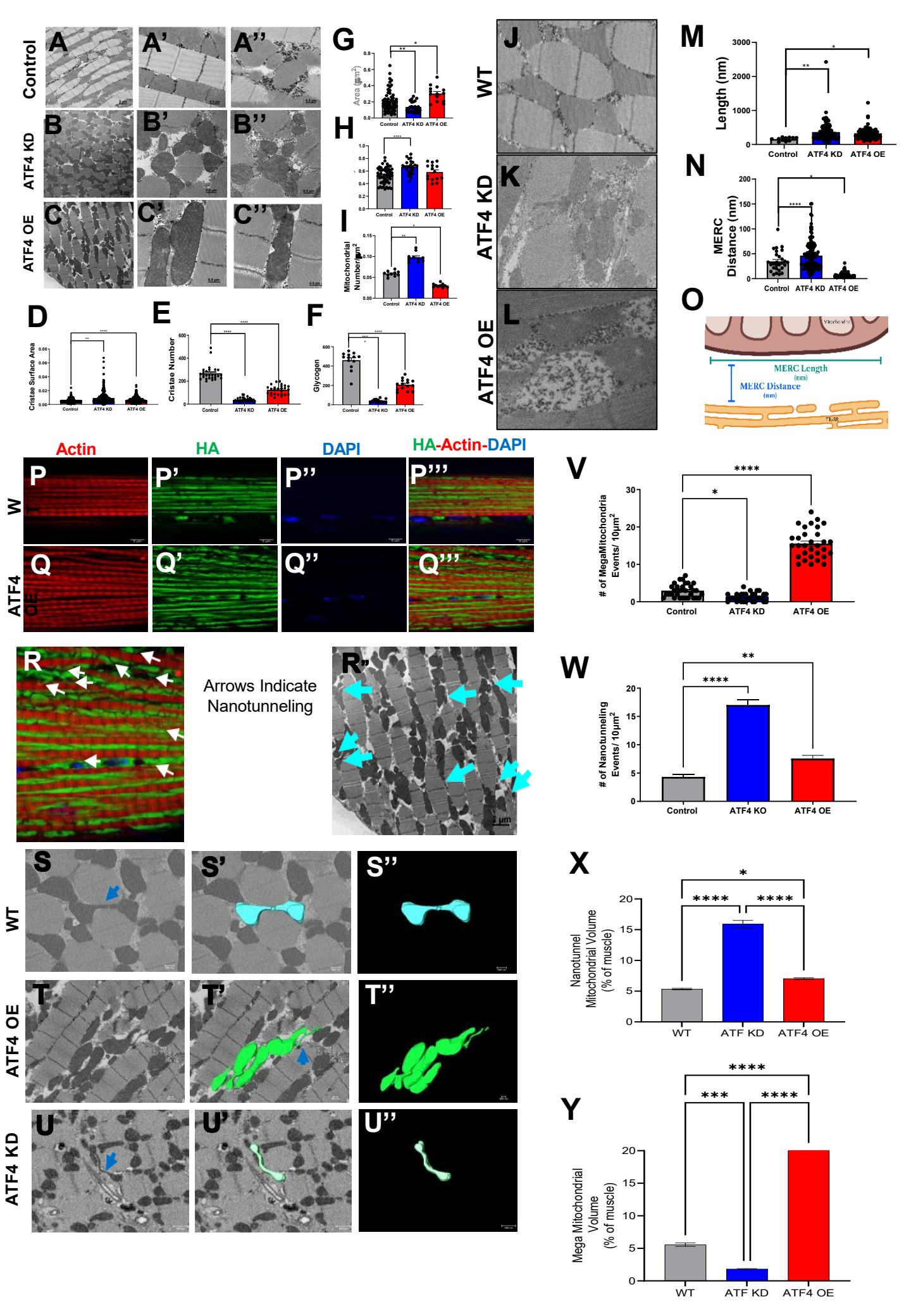
Control
ATF4 KD
ATF4 OE
A
A'
A''
B
B'
B''
C
C'
C''
G
H
I
Area (µm²)
Mitochondrial Number/µm²
Control
ATF4 KD
ATF4 OE
D
E
F
Cristae Surface Area
Cristae Number
Glycogen
ATF4 KO
WT
J
K
L
M
N
O
Length (nm)
MERC Distance (nm)
MERC Length (nm)
MERC Distance (nm)
Actin
HA
DAPI
HA-Actin-DAPI
P
P'
P''
P'''
Q
Q'
Q''
Q'''
V
# of MegaMitochondria Events/ 10µm²
R
R''
Arrows Indicate Nanotunneling
2 µm
W
# of Nanotunneling Events/ 10µm²
S
S'
S''
T
T'
T''
U
U'
U''
X
Nanotunnel Mitochondrial Volume (% of muscle)
Y
Mega Mitochondrial Volume (% of muscle)

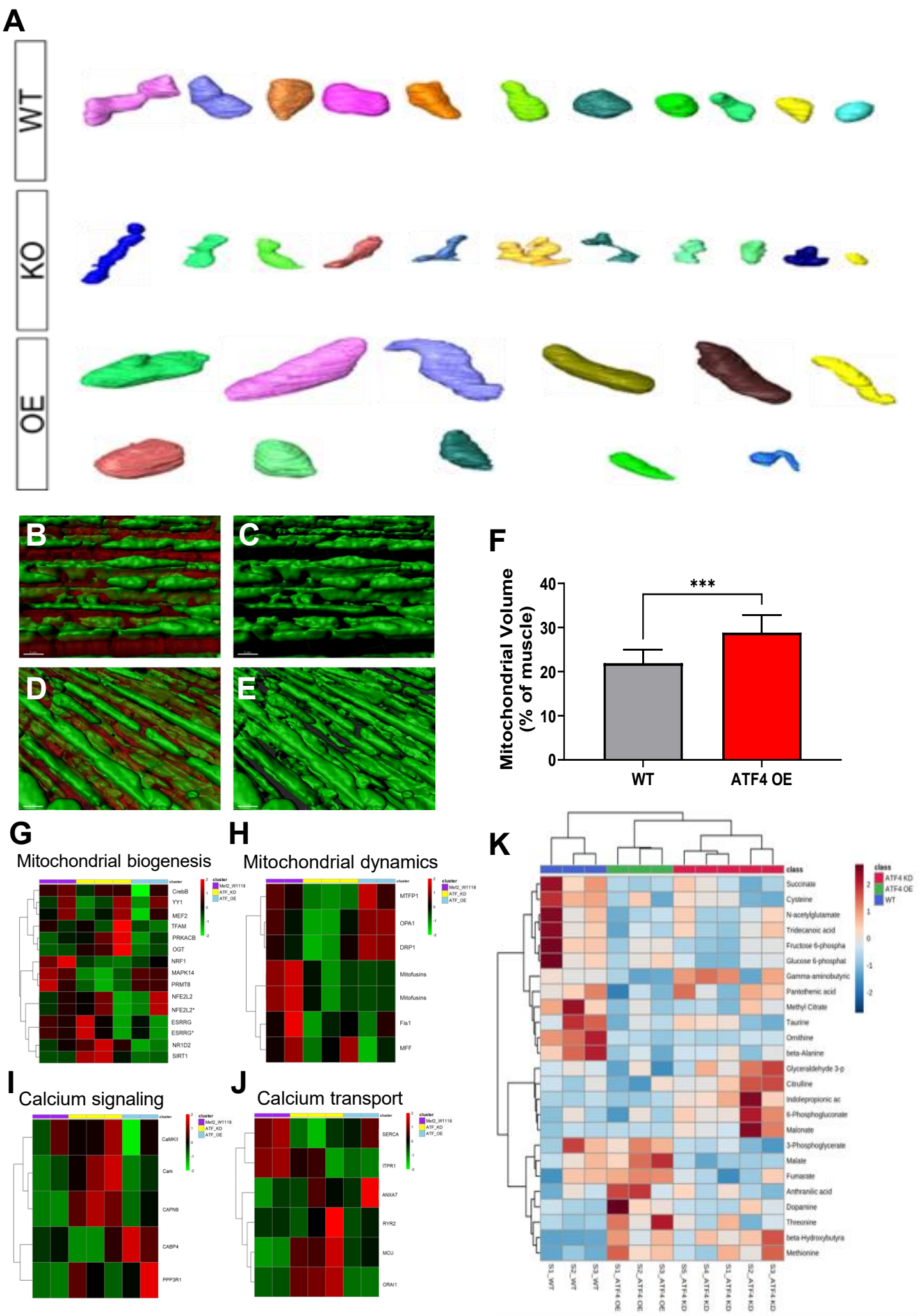
A
WT
KO
OE
B
C
D
E
F
Mitochondrial Volume (% of muscle)
40
30
20
10
0
***
WT
ATF4 OE
G
Mitochondrial biogenesis
CrebB
YY1
MEF2
TFAM
PRKACB
OGT
NRF1
MAPK14
PRMT8
NFE2L2
NFE2L2*
ESRRG
ESRRG*
NR1D2
SIRT1
H
Mitochondrial dynamics
MTFP1
OPA1
DRP1
Mitofusins
Mitofusins
Fis1
MFF
I
Calcium signaling
CaMKII
Cam
CAPN9
CABP4
PPP3R1
J
Calcium transport
SERCA
ITPR1
ANXA7
RYR2
MCU
ORAI1
K
class
ATF4 KD
ATF4 OE
WT
Succinate
Cysteine
N-acetylglutamate
Tridecanoic acid
Fructose 6-phospha
Glucose 6-phosphat
Gamma-aminobutyric
Pantothenic acid
Methyl Citrate
Taurine
Ornithine
beta-Alanine
Glyceraldehyde 3-p
Citrulline
Indolepropionic ac
6-Phosphogluconate
Malonate
3-Phosphoglycerate
Malate
Fumarate
Anthranilic acid
Dopamine
Threonine
beta-Hydroxybutyra
Methionine
S1_WT
S2_WT
S3_WT
S1_ATF4 OE
S2_ATF4 OE
S3_ATF4 OE
S5_ATF4 KD
S4_ATF4 KD
S1_ATF4 KD
S2_ATF4 KD
S3_ATF4 KD

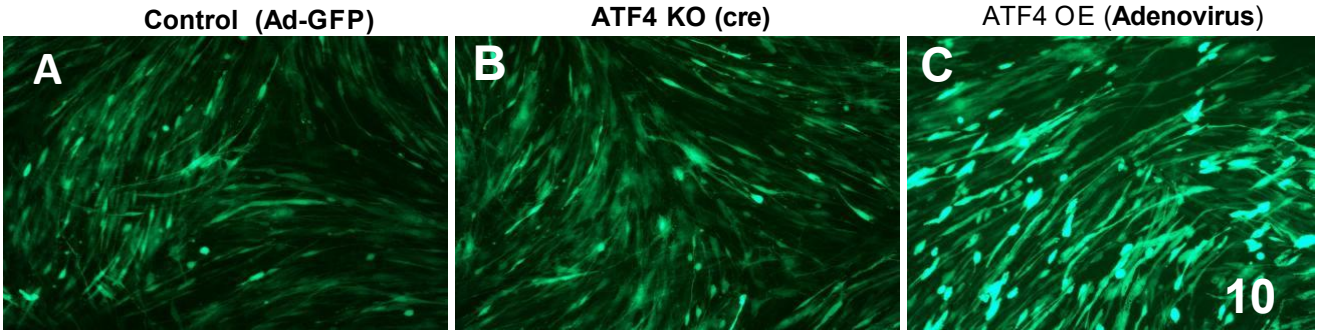
Control (Ad-GFP)
ATF4 KO (cre)
ATF4 OE (Adenovirus)
A
B
C
10

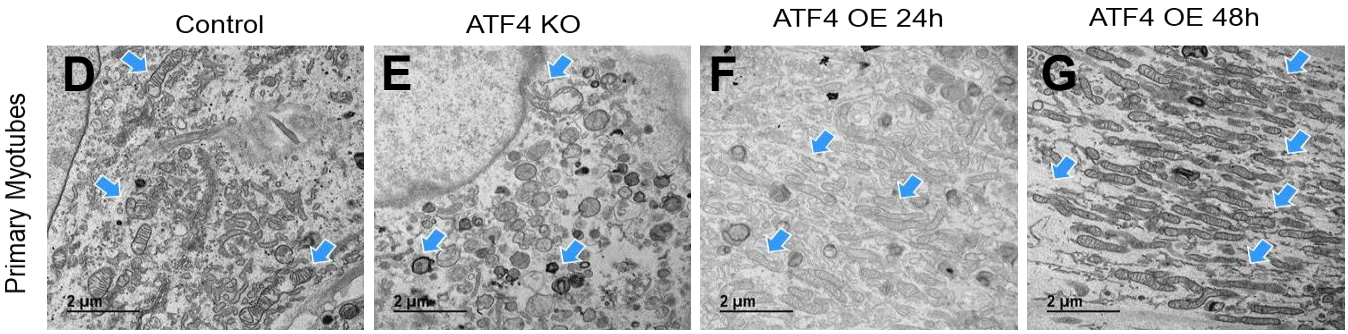
Control
ATF4 KO
ATF4 OE 24h
ATF4 OE 48h
Primary Myotubes
D
E
F
G
2 µm

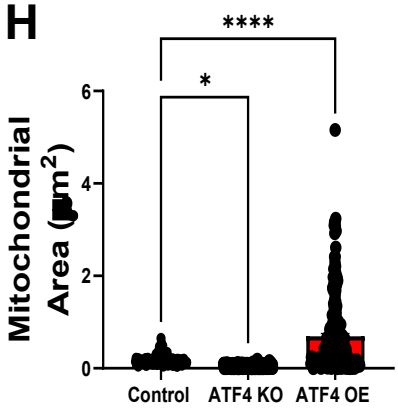
H
Mitochondrial Area (µm²)
****
*
Control
ATF4 KO
ATF4 OE

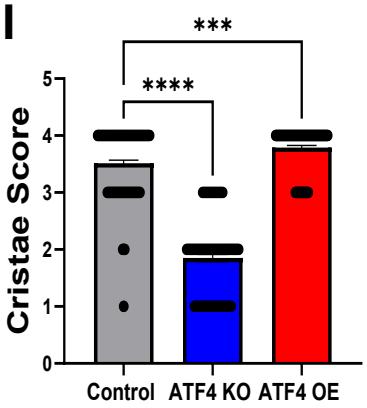
I
Cristae Score
***
****
Control
ATF4 KO
ATF4 OE

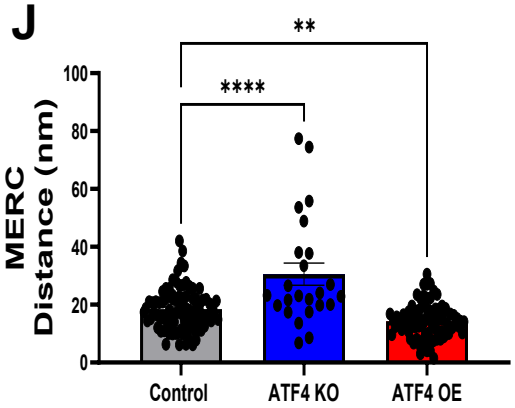
J
MERC Distance (nm)
**
****
Control
ATF4 KO
ATF4 OE

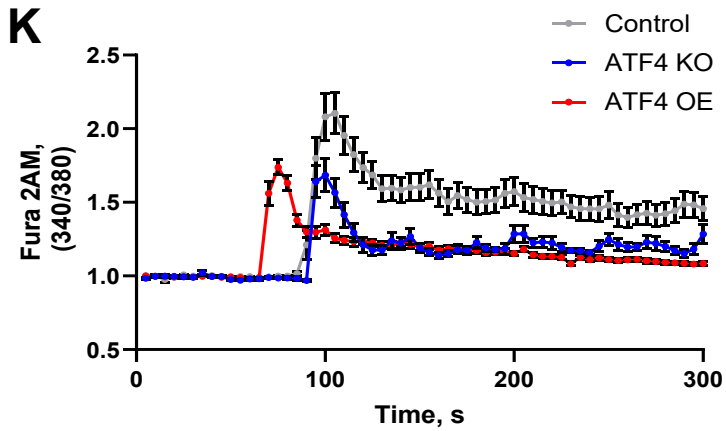
K
Control
ATF4 KO
ATF4 OE
Fura 2AM, (340/380)
Time, s

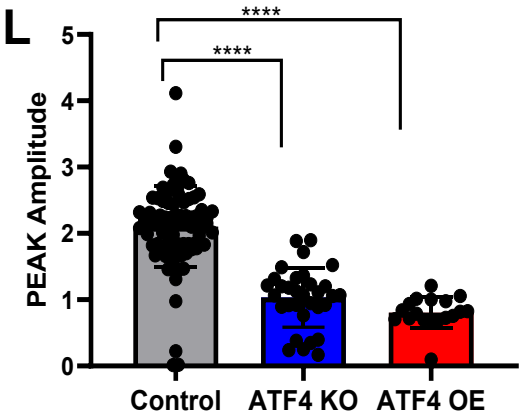
L
PEAK Amplitude
****
****
Control
ATF4 KO
ATF4 OE

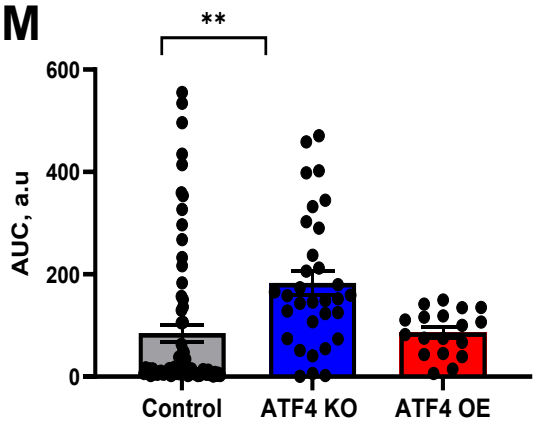
M
AUC, a.u
**
Control
ATF4 KO
ATF4 OE

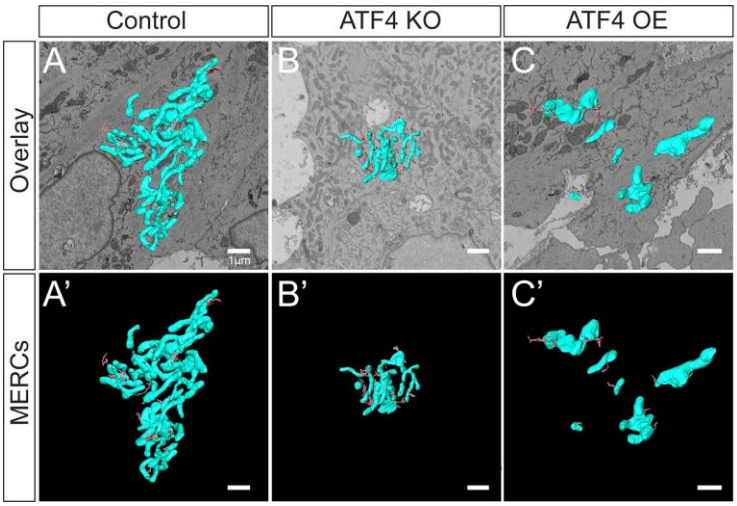
Control
ATF4 KO
ATF4 OE
Overlay
MERCs
A
B
C
A'
B'
C'
1µm

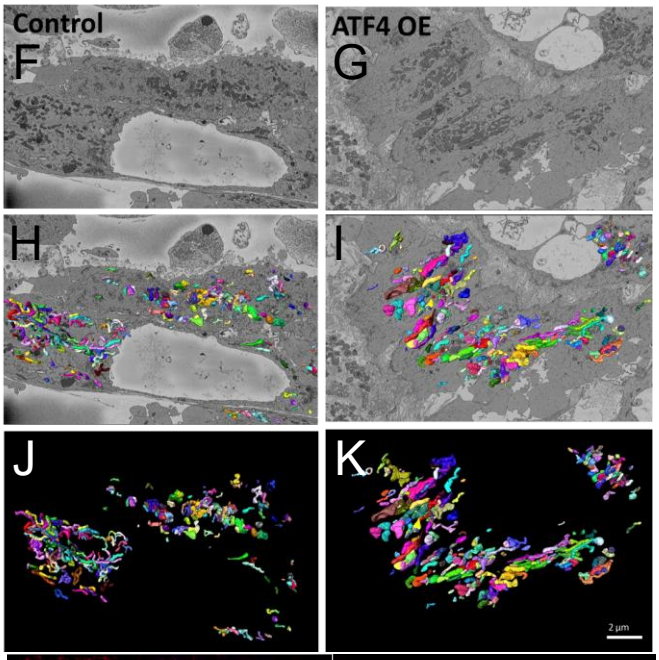
Control
ATF4 OE
F
G
H
I
J
K
2 µm

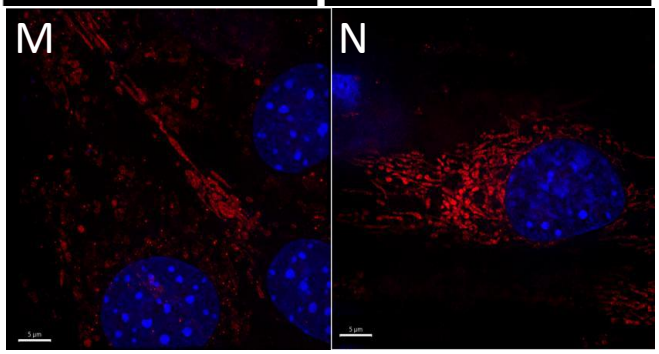
M
N

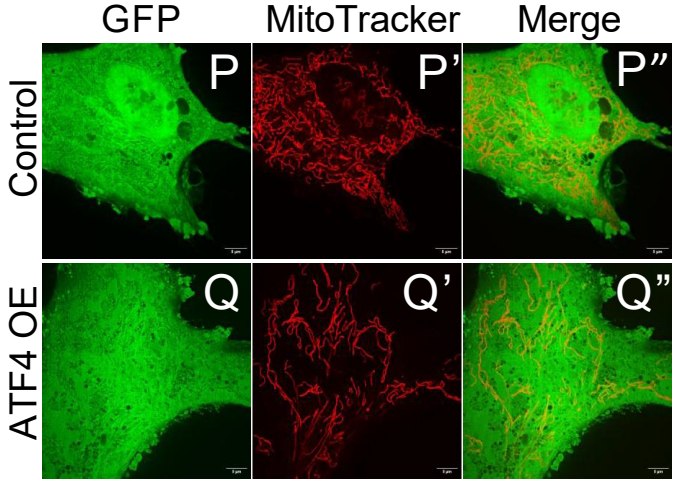
GFP
MitoTracker
Merge
Control
ATF4 OE
P
P'
P''
Q
Q'
Q''

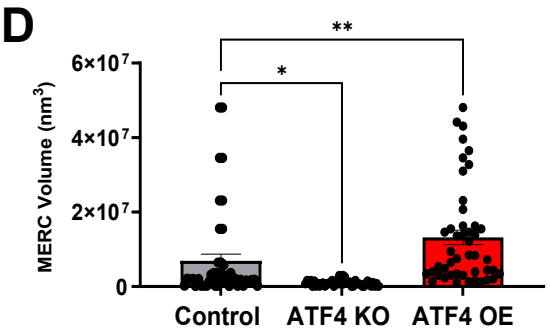
D
MERC Volume (nm³)
6×10⁷
4×10⁷
2×10⁷
0
*
**
Control
ATF4 KO
ATF4 OE

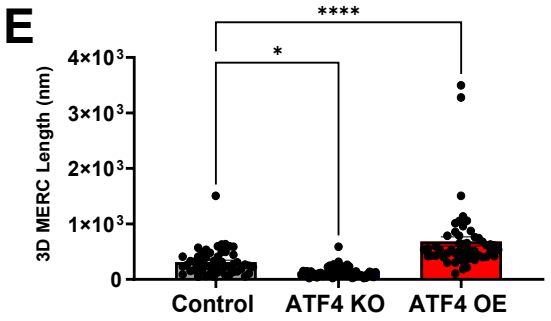
E
3D MERC Length (nm)
4×10³
3×10³
2×10³
1×10³
0
*
****
Control
ATF4 KO
ATF4 OE

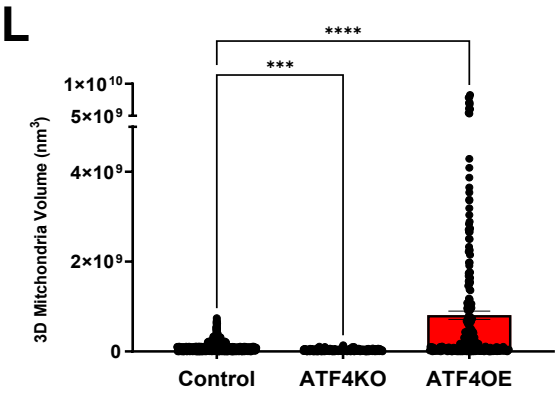
L
3D Mitchondria Volume (nm³)
1×10¹⁰
5×10⁹
4×10⁹
2×10⁹
0
***
****
Control
ATF4KO
ATF4OE

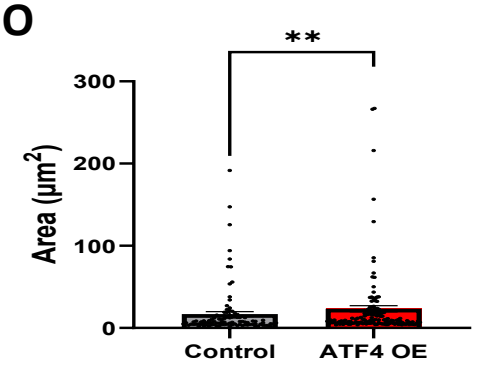
O
Area (µm²)
300
200
100
0
**
Control
ATF4 OE

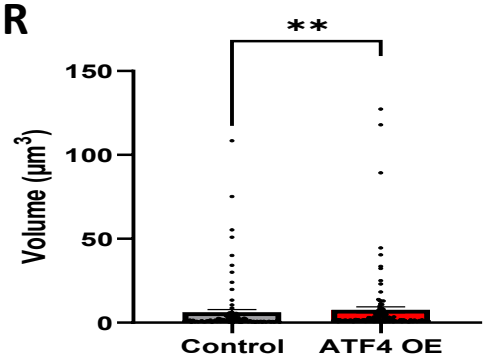
R
Volume (µm³)
150
100
50
0
**
Control
ATF4 OE

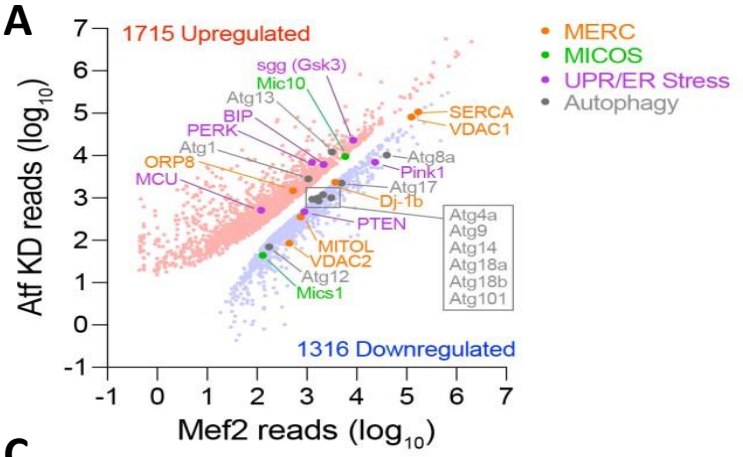
A
1715 Upregulated
1316 Downregulated
MERC
MICOS
UPR/ER Stress
Autophagy
sgg (Gsk3)
Mic10
Atg13
BIP
PERK
Atg1
ORP8
MCU
SERCA
VDAC1
Atg8a
Pink1
Atg17
Dj-1b
PTEN
Atg4a
Atg9
Atg14
Atg18a
Atg18b
Atg101
MITOL
VDAC2
Atg12
Mics1
Atf KD reads (log10)
Mef2 reads (log10)

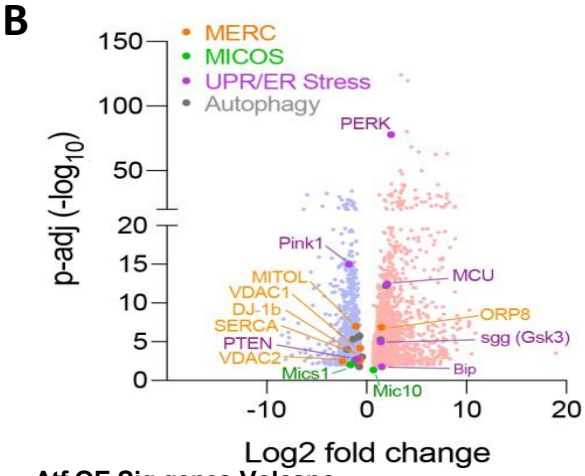
B
MERC
MICOS
UPR/ER Stress
Autophagy
PERK
Pink1
MITOL
VDAC1
DJ-1b
SERCA
PTEN
VDAC2
Mics1
MCU
ORP8
sgg (Gsk3)
Bip
Mic10
p-adj (-log10)
Log2 fold change

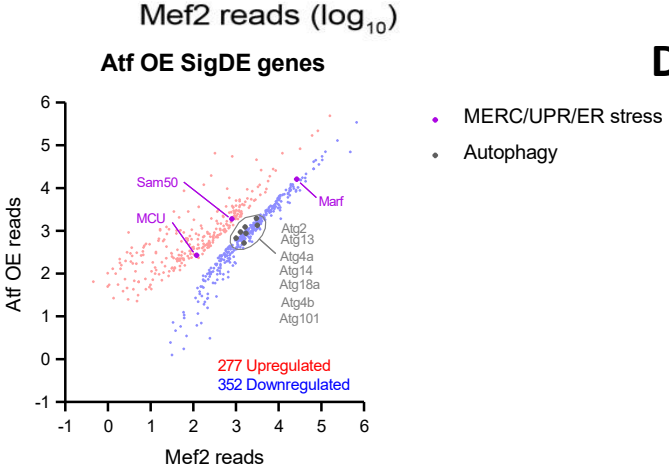
C
Atf OE SigDE genes
MERC/UPR/ER stress
Autophagy
Sam50
MCU
Marf
Atg2
Atg13
Atg4a
Atg14
Atg18a
Atg4b
Atg101
277 Upregulated
352 Downregulated
Atf OE reads
Mef2 reads

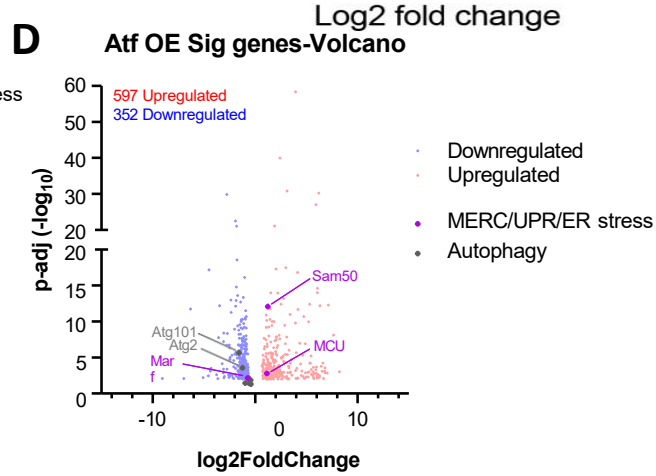
D
Atf OE Sig genes-Volcano
597 Upregulated
352 Downregulated
Downregulated
Upregulated
MERC/UPR/ER stress
Autophagy
Sam50
Atg101
Atg2
Mar
f
MCU
p-adj (-log10)
log2FoldChange

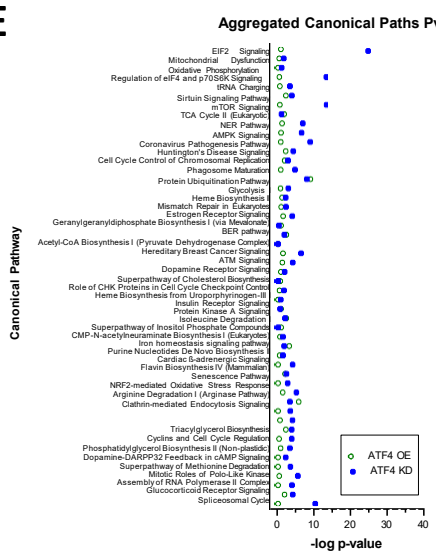
E
Aggregated Canonical Paths Pvalue
Canonical Pathway
ATF4 OE
ATF4 KD
-log p-value

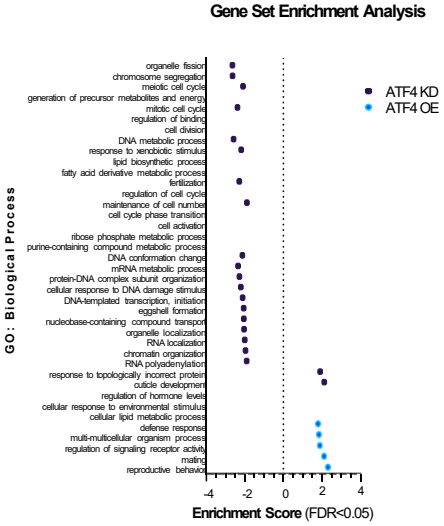
F
Gene Set Enrichment Analysis
ATF4 KD
ATF4 OE
GO: Biological Process
Enrichment Score (FDR<0.05)

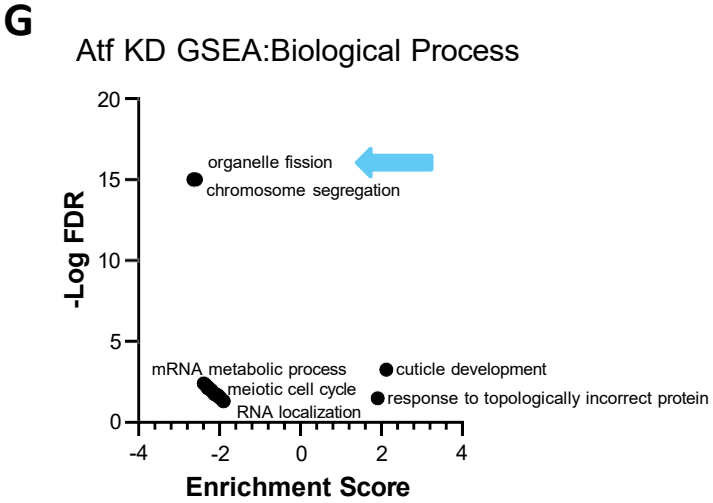
G
Atf KD GSEA:Biological Process
organelle fission
chromosome segregation
mRNA metabolic process
meiotic cell cycle
RNA localization
cuticle development
response to topologically incorrect protein
-Log FDR
Enrichment Score

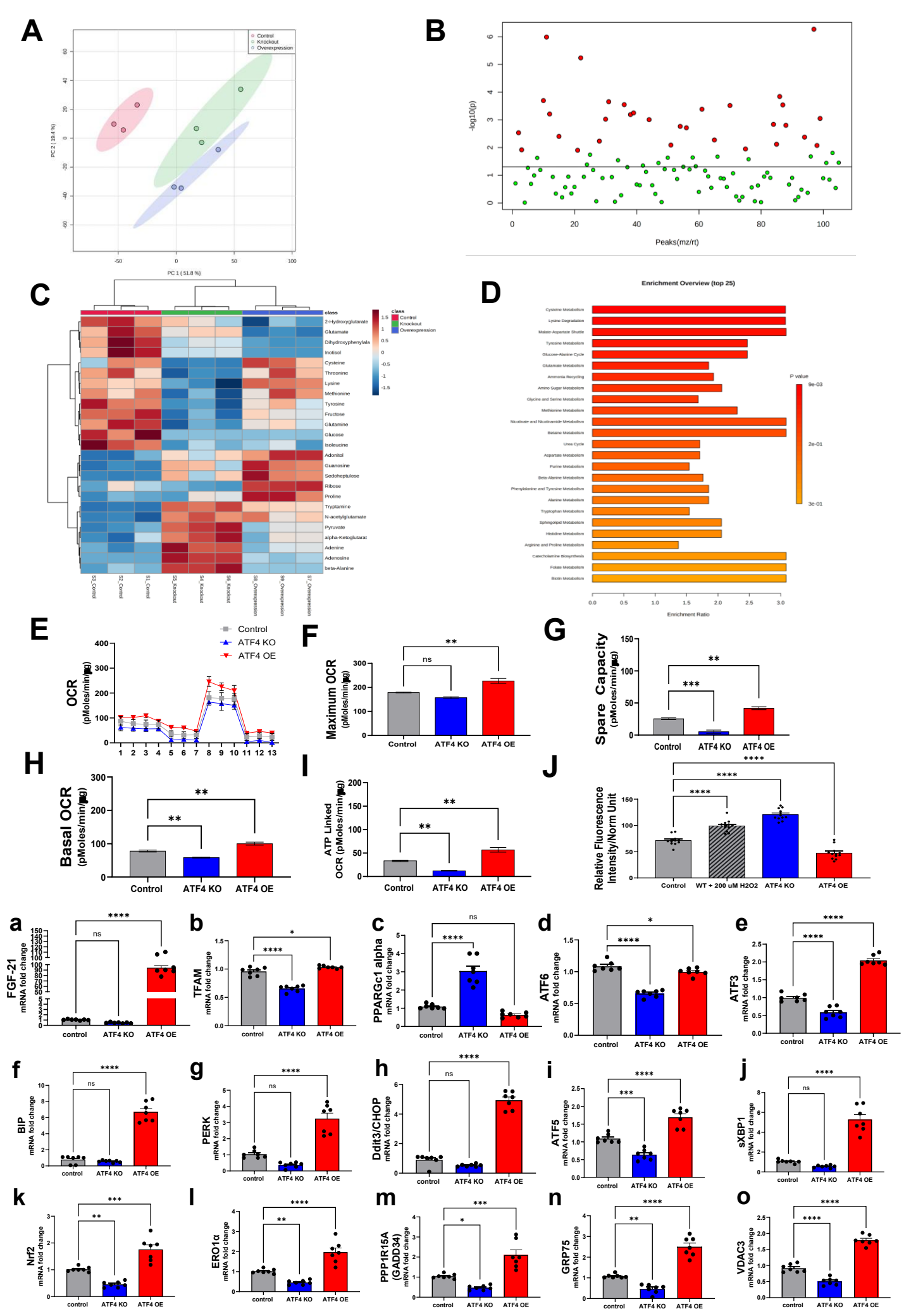
A
Control
Knockout
Overexpression
PC 1 (51.8 %)
PC 2 (19.4 %)
B
-log10(p)
Peaks(mz/rt)
C
class
Control
Knockout
Overexpression
2-Hydroxyglutarate
Glutamate
Dihydroxyphenylala
Inositol
Cysteine
Threonine
Lysine
Methionine
Tyrosine
Fructose
Glutamine
Glucose
Isoleucine
Adonitol
Guanosine
Sedoheptulose
Ribose
Proline
Tryptamine
N-acetylglutamate
Pyruvate
alpha-Ketoglutarat
Adenine
Adenosine
beta-Alanine
D
Enrichment Overview (top 25)
Cysteine Metabolism
Lysine Degradation
Malate-Aspartate Shuttle
Tyrosine Metabolism
Glucose-Alanine Cycle
Glutamate Metabolism
Ammonia Recycling
Amino Sugar Metabolism
Glycine and Serine Metabolism
Methionine Metabolism
Nicotinate and Nicotinamide Metabolism
Betaine Metabolism
Urea Cycle
Aspartate Metabolism
Purine Metabolism
Beta-Alanine Metabolism
Phenylalanine and Tyrosine Metabolism
Alanine Metabolism
Tryptophan Metabolism
Sphingolipid Metabolism
Histidine Metabolism
Arginine and Proline Metabolism
Catecholamine Biosynthesis
Folate Metabolism
Biotin Metabolism
P value
Enrichment Ratio
E
Control
ATF4 KO
ATF4 OE
OCR (pMoles/min/µg)
F
Maximum OCR (pMoles/min/µg)
ns
**
Control
ATF4 KO
ATF4 OE
G
Spare Capacity (pMoles/min/µg)
**
***
H
Basal OCR (pMoles/min/µg)
**
**
I
ATP Linked OCR (pMoles/min/µg)
**
**
J
Relative Fluorescence Intensity/Norm Unit
****
WT + 200 uM H2O2
a
FGF-21 mRNA fold change
b
TFAM mRNA fold change
c
PPARGc1 alpha mRNA fold change
d
ATF6 mRNA fold change
e
ATF3 mRNA fold change
f
BiP mRNA fold change
g
PERK mRNA fold change
h
Ddit3/CHOP mRNA fold change
i
ATF5 mRNA fold change
j
sXBP1 mRNA fold change
k
Nrf2 mRNA fold change
l
ERO1α mRNA fold change
m
PPP1R15A (GADD34) mRNA fold change
n
GRP75 mRNA fold change
o
VDAC3 mRNA fold change
control
ATF4 KO
ATF4 OE

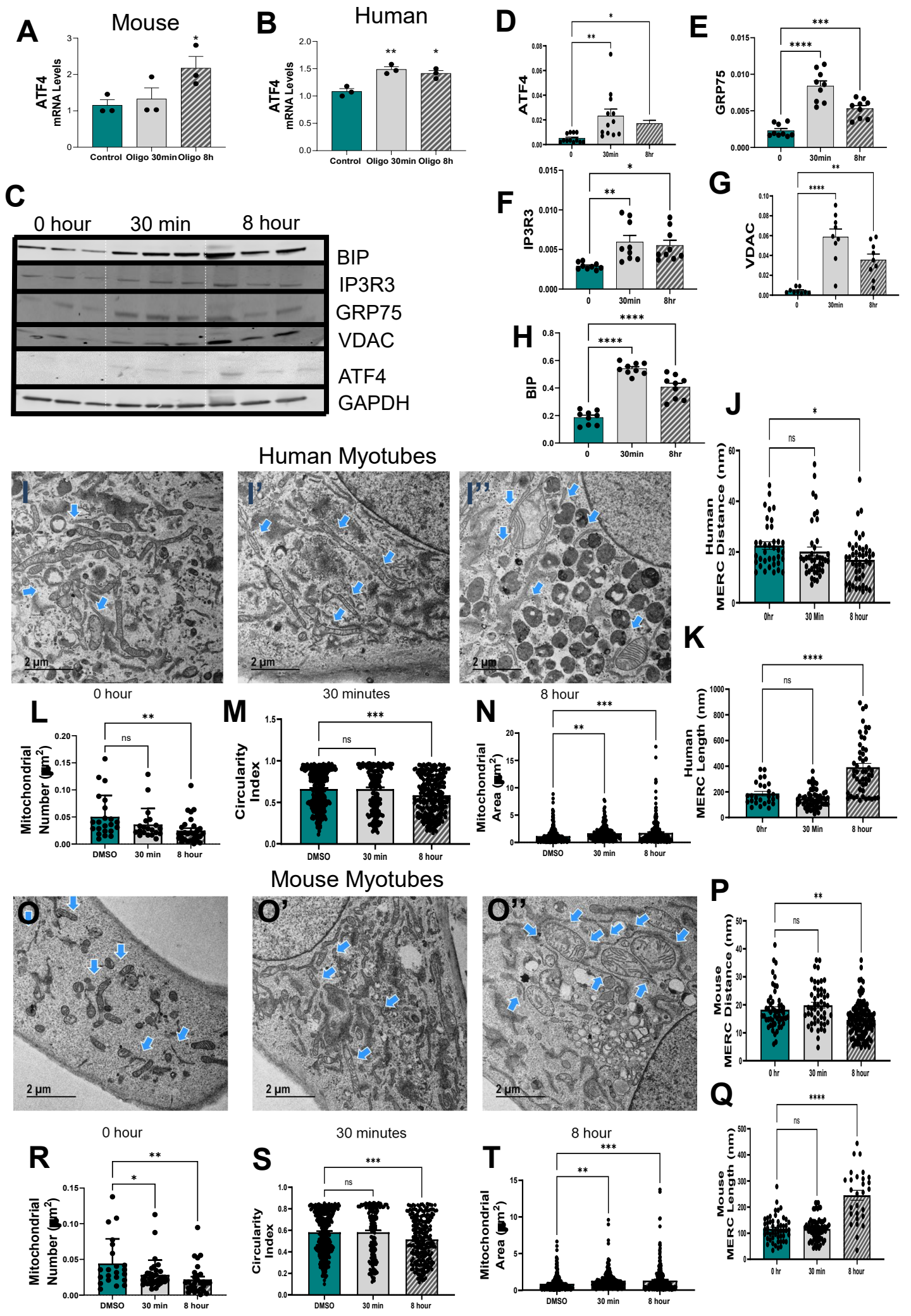
A
Mouse
ATF4 mRNA Levels
Control
Oligo 30min
Oligo 8h
B
Human
ATF4 mRNA Levels
Control
Oligo 30min
Oligo 8h
C
0 hour
30 min
8 hour
BIP
IP3R3
GRP75
VDAC
ATF4
GAPDH
D
ATF4
0
30min
8hr
E
GRP75
0
30min
8hr
F
IP3R3
0
30min
8hr
G
VDAC
0
30min
8hr
H
BIP
0
30min
8hr
J
Human MERC Distance (nm)
0hr
30 Min
8 hour
Human Myotubes
I
I'
I''
2 µm
K
Human MERC Length (nm)
0hr
30 Min
8 hour
0 hour
30 minutes
8 hour
L
Mitochondrial Number (µm²)
DMSO
30 min
8 hour
M
Circularity Index
DMSO
30 min
8 hour
N
Mitochondrial Area (µm²)
DMSO
30 min
8 hour
Mouse Myotubes
O
O'
O''
2 µm
P
Mouse MERC Distance (nm)
0 hr
30 min
8 hour
Q
Mouse MERC Length (nm)
0 hr
30 min
8 hour
0 hour
30 minutes
8 hour
R
Mitochondrial Number (µm²)
DMSO
30 min
8 hour
S
Circularity Index
DMSO
30 min
8 hour
T
Mitochondrial Area (µm²)
DMSO
30 min
8 hour

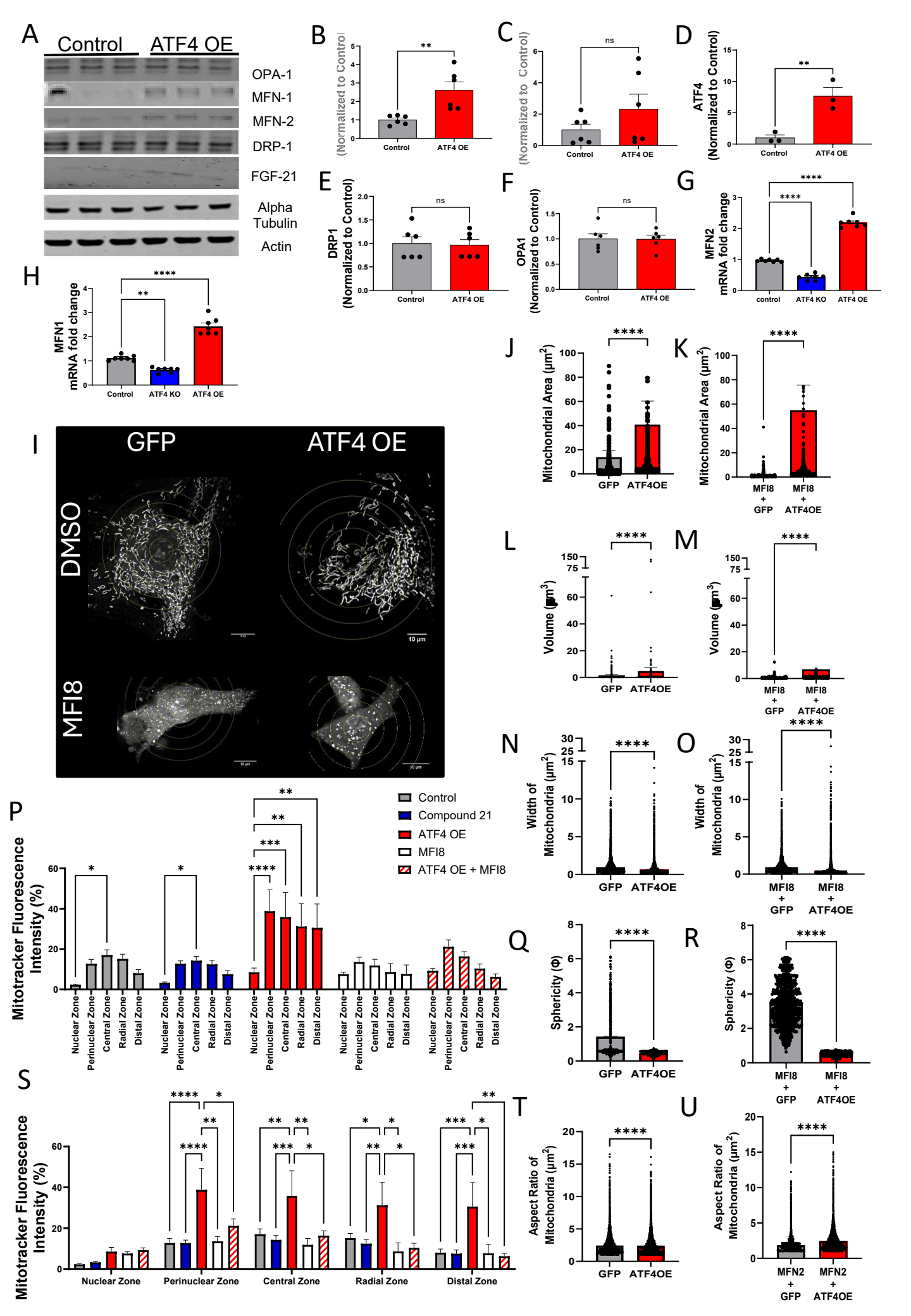
A
Control
ATF4 OE
OPA-1
MFN-1
MFN-2
DRP-1
FGF-21
Alpha Tubulin
Actin
B
(Normalized to Control)
Control
ATF4 OE
C
(Normalized to Control)
ns
D
ATF4 (Normalized to Control)
E
DRP1 (Normalized to Control)
F
OPA1 (Normalized to Control)
G
MFN2 mRNA fold change
control
ATF4 KO
H
MFN1 mRNA fold change
I
GFP
ATF4 OE
DMSO
MFI8
10 µm
J
Mitochondrial Area (µm²)
K
L
Volume (µm³)
M
N
Width of Mitochondria (µm²)
O
P
Mitotracker Fluorescence Intensity (%)
Control
Compound 21
ATF4 OE
MFI8
ATF4 OE + MFI8
Nuclear Zone
Perinuclear Zone
Central Zone
Radial Zone
Distal Zone
Q
Sphericity (Φ)
R
S
T
Aspect Ratio of Mitochondria (µm²)
U
MFN2 + GFP
MFN2 + ATF4OE

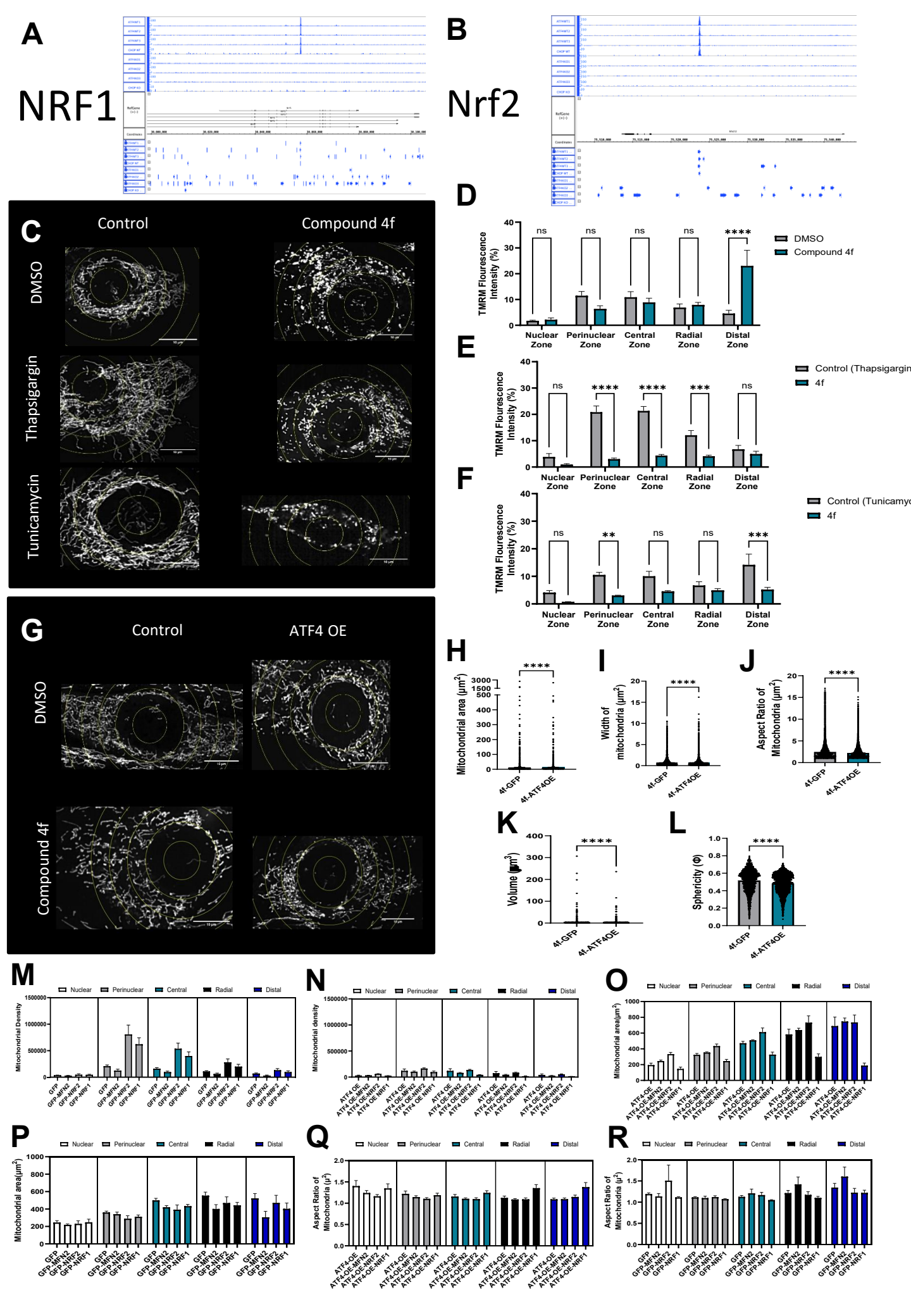
A
NRF1
B
Nrf2
C
Control
Compound 4f
DMSO
Thapsigargin
Tunicamycin
D
TMRM Flourescence Intensity (%)
ns
ns
ns
ns
****
DMSO
Compound 4f
Nuclear Zone
Perinuclear Zone
Central Zone
Radial Zone
Distal Zone
E
TMRM Flourescence Intensity (%)
ns
****
****
***
ns
Control (Thapsigargin
4f
F
TMRM Flourescence Intensity (%)
ns
**
ns
ns
***
Control (Tunicamyc
4f
G
Control
ATF4 OE
DMSO
Compound 4f
H
Mitochondrial area (μm²)
****
4f-GFP
4f-ATF4OE
I
Width of mitochondria (μm²)
****
J
Aspect Ratio of Mitochondria (μm²)
****
K
Volume (μm³)
****
L
Sphericity (Φ)
****
M
Mitochondrial Density
Nuclear
Perinuclear
Central
Radial
Distal
GFP
GFP-MFN2
GFP-NRF2
GFP-NRF1
N
Mitochondrial density
ATF4 OE
ATF4 OE-MFN2
ATF4 OE-NRF2
ATF4 OE-NRF1
O
Mitochondrial area(μm²)
P
Mitochondrial area(μm²)
Q
Aspect Ratio of Mitochondria (μ²)
R
Aspect Ratio of Mitochondria (μ²)